Final Draft
of the original manuscript:

Werwer, M.; Kabir, R.; Cornec, A.; Schwalbe, K.-H.:
Fracture in lamellar TiAl simulated with the Cohesive Model
In: Engineering Fracture Mechanics (2007) Elsevier

DOI: 10.1016/j.engfracmech.2006.09.022

Fracture in lamellar TiAl simulated with the Cohesive Model

M. Werwer, R. Kabir, A. Cornec*), K.-H. Schwalbe

Institute for Materials Research,
GKSS Research Center – Member of the Helmholtz Association,
Max–Planck–Straße 1, D-21502 Geesthacht, Germany

Abstract

Fracture behaviour of lamellar TiAl is studied by means of experiments and numerical simulations using a cohesive model. The fracture process can be described by two cohesive parameters: traction, T_0, and separation work, Γ_0. These are identified for polysynthetically twinned crystals (PST) and a polycrystalline TiAl alloy by comparison of the numerical simulations with experimental fracture tests. The appropriate shape of the traction-separation law for quasi-brittle fracture was identified. The simulation of the PST crystal deformation is based on crystal plasticity including the specific lamellar orientation relations. In a PST crystal, fracture occurs by inter- and translamellar fracture. In an extruded polycrystal, the lamellae of the colonies are randomly aligned in radial direction but more uniformly in extrusion direction for which different fracture toughness values are obtained. For the polycrystalline γTiAl conventional J_2 plasticity is applied, which seems appropriate to predict macroscopic effects either for stable crack extension or unstable failure. The cohesive separation, δ_0, can be interpreted as a characteristic length for a representative microstructural volume.

Key words: Titanium aluminide alloy; PST crystal; Lamellar microstructure; Cohesive model, Finite element method

---

* Corresponding author. Tel.: +49-4152-87-2535; Fax: +49-4152-87-2534,
E-mail address: cornec@gkss.de (A. Cornec).

Notation

Variables

a	Crack length (a_0 initial crack)
a/W	Crack length to width ratio
v_{LL}	Force-displacement
B	Thickness of bend specimen
$CMOD$	Crack mouth opening displacement
F	Force
F_Y	Yield force
J_i	Fracture toughness for crack initiation, expressed by the J-integral
K_{Ic}	Fracture toughness, expressed by the stress-intensity factor
L_S	Lamellar thickness
S	Loading span width of bend specimen
$T(\delta)$	Traction-separation function (TSL)
T_0	Maximum separation stress
W	Width of bend specimen
δ	Separation parameter
δ_1, δ_2	Cohesive shape parameters
δ_0	Maximum separation
φ	Orientation angle of the lamellae with respect to loading direction
σ_Y	Yield strength
Γ_0	Maximum separation work
L_R	Height of a representative volume at fracture
L_S	Average thickness of γ-lamellae

Acronyms

CRSS	Critical resolved shear stress
PST	Poly-synthetically twinned TiAl alloy
TD	Transverse orientation of polycrystal fracture (crack plane transverse to extrusion direction)
LD	Longitudinal orientation of polycrystal fracture (crack plane longitudinal to extrusion direction)
TSL	Traction separation law

1. Introduction

γ-based titanium aluminide alloys (γTiAl) with preferentially lamellar microstructures are novel high-temperature light-weight structural materials and have a great potential for automobile and aerospace applications [1]. γTiAl alloys combine a number of attractive properties such as high specific stiffness and specific strength, good oxidation and creep resistance. Like other intermetallic alloys, however, γTiAl alloys suffer still from poor ductility and fracture toughness.

Based on experimental experience, micromechanical related models have been proposed by Chan [2-4], Chan and Kim [5] and simulations performed by Arata et al. [6-8] to improve the mechanical understandig about fracture behaviour of lamellar TiAl.

Chan has proposed the analytical shear ligament model. This model is based on the assumption that damage in the lamellar colonies occurs by interlamellar fracture. Due to the misalignments of the lamellar orientations of adjacent colonies, shear ligaments are formed. The fracture resistance is enhanced by plastic dissipation within the shear ligaments. For small colony size shear ligament effects diminish.

Arata et al. have performed micromechanical simulations of a 2D representation of a fully-lamellar microstructure of large colonies. Interlamellar fracture was described with a cohesive model. Arata et al. have shown, that the fracture resistance is enhanced by the inclination of the lamellar orientation between neighbouring colonies. The source for this enhancement is addressed to the hindrance exerted by colony boundaries.

The evidently very low fracture toughness range for interlamellar fracture ($K_{Ic} \approx$ 2-4 MPa√m) makes the γTiAl very sensitive against force-displacement behaviour of a component. The weak interlamellar crack path occurs only for orientation angles between loading axis and lamellar plane within approximately φ = 80°-90°. The other orientations of the lamellar planes will exhibit predominantly translamellar fracture. Along the boundaries of the lamellar colonies fracture initiation or cracking are not observed. Hence, for an isotropic polycrystal, series of colonies oriented for creating pure interlamellar fracture are statistically relatively rare, as for example, within an orientation space between φ = 0° and 180° only 2 colonies for φ = 80°-90° are preferentially oriented for pure interlamellar colony fracture while the others within φ = 0°-70° are dominated by translamellar fracture. Thus, γTiAl exhibits not necessarily a weak fracture resistance. In practice, alloy designers try to avoid colonies oriented for interlamellar fracture to benefit from the higher fracture toughness of translamellar fracture. In extruded bars, lamellar orientations are aligned in extrusion directions,

where a fraction of quasi-interlamellar fracture may reduces pure translamellar fracture toughness.

In the present work, the fracture mechanisms in lamellar γTiAl are studied by means of numerical simulations using a phenomenological cohesive model. The constitutive cohesive traction-separation law (TSL) is defined by two parameters, the maximum traction, T_0, and the maximum separation work, Γ_0. These two cohesive parameters are identified by comparing numerical fracture simulations with experimental data from poly-synthetically-twinned (PST)[1] crystals and from a polycrystalline γTiAl alloy. The simulation of the PST crystal deformation is based on crystal plasticity including the specific lamellar orientation relations. For the polycrystal TiAl conventional J_2 plasticity is applied, although local crystal slip systems near the crack tip may develop differently. But it seems appropriate for the macroscopic effects of stable crack extension up to unstable failure predictions.

In addition, the relevant shape of the TSL for quasi-brittle fracture has been identified.

2. Deformation and fracture mechanisms in lamellar TiAl

γ-TiAl alloys consist of the two intermetallic phases, α_2 (Ti_3Al) and γ (TiAl). The γ-phase is generally the majority phase with a volume fraction of 80-98%, depending on the actual chemical composition of the alloy. The crystallographic structures of the α_2- and γ-phases are the hexagonal $D0_{19}$ and the tetragonal $L1_0$ structure, respectively, as depicted in Fig. 1. The lamellar substructure is formed according to the orientation relationship $(0001)_{\alpha_2} \parallel \{111\}_\gamma$ and $\langle 11\bar{2}0\rangle_{\alpha_2} \parallel \langle 111\rangle_\gamma$. Six orientation variants of the γ-phase fulfil the orientation relationship. These can be divided into 3 matrix orientations with $\langle 11\bar{2}0\rangle_{\alpha_2} \uparrow\uparrow \langle 110\rangle_\gamma$ and 3 twin orientation with $\langle 11\bar{2}0\rangle_{\alpha_2} \uparrow\downarrow \langle 110\rangle_\gamma$, where ↑↑ and ↑↓ denote parallel and anti-parallel relations, respectively. The notations used are as follows: { } and ( ) represent slip planes, where ( ) are specific ones, ⟨ ⟩ and [ ] represent slip directions, where the last is used for specific slip orientations. The relevant lamellar substructure of γTiAl is schematically shown in Fig. 2(a).

Plastic deformation occurs in the α_2-phase by crystallographic slips systems: prismatic

[1] In a PST crystal numerous thin-related lamellae are contained in major constituent γ-phase of the crystals, these crystals are called polysynthetically twinned (PST) crystals from analogy with the phenomenon of polysynthetical in mineral crystals.

$\langle 11\bar{2}0\rangle\{1\bar{1}00\}$, basal $\langle 11\bar{2}0\rangle$ (0001) and pyramidal $\langle\bar{1}\,\bar{1}26\rangle$ $\{11\bar{2}1\}$. The critical resolved shear stresses in the α_2-phase have been determined e.g. by Inui [9] as 100, 330, and 910 MPa, respectively.

In the γ-phase, slip occurs on the {111} habit planes by ordinary dislocations $1/2\langle 110]$, superdislocations $\langle 011]$ and $1/2\langle 11\bar{2}]$ and by mechanical twinning due to $1/6\langle 11\bar{2}]$ partial dislocations. The individual slip systems of the γ-phase in lamellar γTiAl can be classified morphologically into the longitudinal, mixed and transverse slip modes as proposed by Lebensohn [10]. Longitudinal slip occurs on a longitudinal plane (i.e. parallel to the lamellar interface) in a longitudinal direction. Mixed slip is on a transverse plane (i.e. across the lamellar interface) in a longitudinal direction. Transverse slip is on a transverse plane in a transverse direction. These slip systems are depicted in Fig. 2(b). The CRSS for this longitudinal, mixed and transverse slip modes have been previously experimentally determined for a PST crystal as 55, 150 and 185 MPa, respectively, [11].

Fracture in γTiAl occurs by cleavage along the habit planes. The cleavage planes are the close-packed crystallographic planes $\{111\}\gamma$ and $(0001)\alpha_2$ as well as the closely packed parallel directions $\langle 1\bar{1}0]_\gamma$ and $\langle 11\bar{2}0\rangle_{\alpha_2}$. Depending on the orientation relationship of the lamellae, fracture can take place in an interlamellar manner along lamellar planes of α_2/γ as well as in an translamellar mechanism along γ/γ planes (γ is either the matrix or twin).

Due to the different lamellar orientations a fully-lamellar polycrystal cannot completely fail solely by pure interlamellar cleavage fracture like a PST. Translamellar fracture occurs mainly on short transverse $\{111\}_\gamma$ planes, where lamellar boundaries act as natural barriers for crack path deviations which enhances fracture toughness considerably compared to perfect interlamellar fracture on a long habit plane. Nevertheless, the fracture toughness may be unique for all $\{111\}_\gamma$ planes. Thus, global fracture behaviour depends on the microstructural texture, namely concentration and alignment of similar lamellar orientations. The texture can be induced for example by an extrusion process.

3. Experimental

A PST crystal was grown from an remelted round specimen (9 mm diameter, 68 mm long) taken from an ingot of a binary TiAl alloy with the composition Ti-49.3Al (at.%).

In such a PST crystal numerous thin lamellae are received in the major constituent γ-phase and is now commonly referred to as a polysynthetically twinned crystal. The lamellar spacing of this PST crystal was in the range of 1-5 μm. The PST round bar was machined in the facility at the Technical University Hamburg-Harburg as described by Uhlenhut [11].

For the PST crystal fracture tests, small sized bend specimens are prepared. Inside the bend specimens, PST kernels were electrodischarge machined from the PST round bar and oriented for interlamellar and translamellar fracture, as shown in Fig. 3. The dimensions of the PST kernels were 4.5 mm wide, 2.25 mm thick and 4.95 mm long. The PST kernels were diffusion bonded to polycrystalline TiAl grips. Crack-like slits of about 60-70 μm width were electrodischarge machined into the PST kernel. The crack length aspect ratio was a/W = 0.35. These small bending specimens were used for testing in an apparatus with in-situ observations in a scanning electron microscope. The γ-lamellae have a thickness of about 2 μm.

For the polycrystal fracture tests, same small sized specimens were prepared from the extruded GKSS alloy γTAB with the composition Ti-47Al-3.7(Nb,Cr,Mn,Si)-0.5B.

After ingot casting, an extrusion process followed with a reduction ratio of 7:1 forming a round bar of Ø22mm. The lamellar microstructure is obtained through heat treatment at 1360 °C for 30 min followed by oil-cooling in order to get a fine-grained fully lamellar microstructure, where a mean colony size of approximately 100 μm was obtained with a mean lamellar thickness somewhat less than 1 μm. Stress relaxation is ensured by heating up to 800 °C for 6h followed by air-cooling. The previous extrusion process is responsible for anisotropic orientations of the lamellar colonies. Due to the crystallographic $\{111\}_\gamma$ habit planes of the γ-phase during the extrusion flow the lamellae recrystallise nearly parallel to the extrusion direction, while in the radial section of the extruded bar they are oriented almost randomly (i.e. quasi-isotropic), as depicted in Fig. 4(a).

Flat bar tensile specimens as well as bend specimens of the orientations TD (crack plane transverse to the extrusion direction) and LD (crack plane longitudinal to the extrusion direction) were electrodischarge machined from the γTAB bar, Fig. 4(b). The orientations of the fracture planes are placed in the two directions TD and LD in Fig. 4(c). The dimensions of the flat bar specimen with a square test section are given in Fig. 4(d). The small sized bend specimens are shown in Fig. 4(e), having a crack like slit of 60-70 μm width. Two crack length ratios were prepared, a/W = 0.35 and 0.6 for the orientation TD, and a/W = 0.6 only for the LD.

4. Numerical

For the deformation and fracture simulations of the PST crystals, multi-scale simulations (denoted commonly as FE^2) for the PST crystal were performed as described in previous works [12-15]. In FE^2 simulations, a periodic unit cell contains the constitutive behaviour and is more complex than those in standard FE-methods. More general details on the FE^2 method can be found in the work of Feyel and Chaboche [16].

A representative volume element of the constituents of γTiAl is shown qualitatively in **Fig. 5(a)**. For the FE^2 simulations, an idealized periodic unit cell was used, consisting of one α_2-lamella, one γ-matrix and one γ-twin lamella, as shown in Fig. 5(b). The plastic deformation within each lamella was described by continuum crystal plasticity based on Asaro's work [17]. For the α_2-lamella, the prismatic, basal and pyramidal slip systems were taken into account as described in section 2. For the γ-lamellae, the deformation behaviour of the three γ-matrix and the three γ-twin domain orientations, respectively, was homogenized, Fig.5(b). Due to this homogenization, twinning, the superdislocations $1/2\langle 01\bar{2}]$, and any sophisticated differences between the ordinary $1/2\langle 110]$ and superdislocations $\langle 011]$ were neglected. Therefore, only longitudinal, mixed and transverse dislocations [110] were taken into account.

The translamellar fracture process in a PST crystal as shown in Fig. 6(a) is idealized by the cohesive model. The general concept of the cohesive model is schematically shown in Fig. 6(b). The cohesive model desribes basically the separation, δ, of a material due to action tractions, T. For crack initiation and propagation, the cohesive model assumes that any material volume ahead of the crack tip undergoes the same traction–separation history. Thus, the fracture mechanisms in the process zone may therefore be described by a uniform TSL, which has the following three characteristic functions $T(\delta)$:

$$\frac{T}{T_0} = \begin{cases} 2\left(\dfrac{\delta}{\delta_1}\right) - \left(\dfrac{\delta}{\delta_1}\right)^3 & \text{for } \delta \le \delta_1 \\ 1 & \text{for } \delta_1 \le \delta \le \delta_2 \\ 2\left(\dfrac{\delta-\delta_2}{\delta_0-\delta_2}\right) - 3\left(\dfrac{\delta-\delta_2}{\delta_0-\delta_2}\right)^3 + 1 & \text{for } \delta_2 \le \delta \le \delta_3 \end{cases} \tag{1}$$

The cohesive model and the TSL are implemented into the FE code ABAQUS [18] by user defined elements (UEL) as developed by Scheider [19-21]. The formulations are valid for several types of elements.

The TSL above contains only two characteristic parameters, a cohesive strength, T_0, and a critical separation, δ_0. However, the shape of the TSL is not yet resonably justified. It has to be identified by simulations compared to experimental measurements of the global behavior of specimens with particular fracture phenomena, e.g. quasi-brittle or ductile.

Two limiting shapes for the TSL are important, which are controlled by the parameters δ_1 and δ_2, i.e. a quadratic (trapezoidal) shape (Quad-TSL), Fig. 7(a), and a triangular shape (Tria-TSL), Fig. 7(b). The shape parameters for Quad-TSL are fixed to $\delta_1 = 0.001\delta_1$ and $\delta_2 = 0.75\delta_1$ and for the Tria-TSL δ_2 is set close or equal to δ_1. The elastic stiffness of the cohesive element is given by δ_1. The softening behaviour is represented between δ_2 and δ_0. If δ exceeds δ_0, the cohesive element cannot transmit stresses any more and a new surface is created and the crack has extended by one element width. In the FE-model, interface elements are introduced between continuum elements, as schematically shown in Fig. 7(c).

Instead of the maximum separation, δ_0, the TSL can also be characterized in terms of separation work Γ_0, which is the area under the traction-separation curve:

$$\Gamma_0 = \int_0^{\delta_0} T(\delta)\,\mathrm{d}\delta \tag{2}$$

The maximum separation, δ_0, is related to T_0 and Γ_0 as follows

$$\delta_0 = \frac{2\Gamma_0}{T_0\left(1 - \frac{2}{3}\frac{\delta_1}{\delta_0} + \frac{\delta_2}{\delta_0}\right)} \tag{3}$$

The two cohesive parameters, T_0 and Γ_0, can be determined from tests. The traction, T_0, is equal to the maximum true stress at fracture of a tensile specimen and the separation work, Γ_0, is equal to crack initiation from fracture tests [22]. They can also be fitted to load-displacement records of specimens, for example as demonstrated in [23] for brittle type materials.

For the FE^2 simulations of the PST deformation and fracture behaviour, this cohesive model was implemented on surfaces of each 3D unit cell, Fig. 5(b). For the FE^2 simulations only the Quad-TSL was used, Fig. 7(a).

Standard FE-methods were applied to the macroscopical fracture behaviour of the polycrystal γTAB. FE^2 simulations with grain sized unit cells including fracture are not

yet established. The deformation behaviour of the polycrstalline γTAB was described by J_2 plasticity using a mean stress–strain curve obtained from tensile tests. The simulations were performed under 2D plane strain conditions.

5. Results

5.1 General aspects

The aim of the results presented below is focused on the validation of the cohesive model using force-displacement curves of precracked bend specimen under displacement control. An approach will be presented on how the cohesive parameters, T_0 and Γ_0, can be determined by simulations.

First, the cohesive traction, T_0, is varied in combination with the limiting case $\Gamma_0 \to \infty$, i.e. no fracture will occur in these curves. This parameter setting is related to a stress-stain curve truncated at $\sigma = T_0$ and beyond infinitely elongated on an ideal-plastic level. From the variations of T_0 (with $\Gamma_0 \to \infty$) the most appropriate value for T_0 can be discerned by comparing the numerical curves with the experimental curve in the initial increasing force range before maximum force is reached.

In a next step the cohesive work, Γ_0, is varied with the previously fixed T_0 values. These curves allow a final decision of the most appropriate cohesive parameter, Γ_0. A more refined parameter setting for T_0 and Γ_0 can be simply interpolated from the characteristics of the initial curves.

The values for Γ_0 can also be experimentally determined at the loading stage where physical crack initiation occurs. Fracture toughness at crack initiation can be determined using the *J*-integral with the expression

$$J_i = \frac{2A}{B\left(W - a_0\right)} \tag{4}$$

where A is the area under the force-displacement curve. This J_i-value can be used as geometry independent initiation values if the size requirements

$$25\frac{J_0}{\sigma_Y} \geq B \text{ and } \left(W - a_0\right) \tag{5}$$

are fulfilled. For the given specimen sizes, the maximum J-value for the smallest ligament (W-a_0) = 0.4W and σ_Y = 400 MPa can be J_{max} = 29 N/mm, which is well above all results obtained for Γ_0 on PST and γTAB.

In the elastic fracture regime the J-integral at initiation can be converted to a critical fracture toughness value, K_{Ic}, expressed by the stress intensity factor

$$K_{Ic} = \sqrt{E' J_i} \tag{6}$$

with $E' = E/(1-\nu^2)$ for 2D plane strain condition and ν as the Poission ratio. Analytical solutions for the stress-intensity factor, K, as well crack opening displacements for bend specimens under three point bending can be found in [24,25]. The elastic modulus is E = 175000 MPa for both, the PST and γTAB.

With the equivalence $\Gamma_0 = J_i$ any Γ_0 value can be converted to K_{Ic}, if the above requirements are fulfilled. Assuming K_{Ic} = constant for quasi-static crack extension in the elastic regime a force-displacement curve can be analytically formulated depending on the increasing crack length. Such analytical curves are presented and compared with simulated curves using the cohesive model, which also assumes Γ_0 = constant during crack extension.

A further general aspect is the yield force, F_Y, which is helpful to identify in which regime fracture takes place, i.e. under elastic, contained yielding or fully plastic yielding. The yield force, F_Y, for the bend specimen is as follows

$$F_Y = \beta \frac{B(W-a)^2}{S} \sigma_Y \tag{7}$$

β is a factor for 2D plane stress or plane strain conditions (with β = 1.072 for plane stress as a lower, β = 1.456 for plane strain as an upper bound). The initial part of the force-displacement curve (up to F_Y) cannot be described accurately enough with the elastic compliance alone. However, the effective crack length, a_{eff}, which contains a plastic zone size correction, yields a good approximation of the slight nonlinearity of the curve. The plastic zone size correction under small-scale yielding conditions can be considered by the well known approximation

$$r_p = \frac{1}{2\pi}\left(\frac{K(a_0)}{\sigma_Y}\right)^2 \tag{8}$$

and with this contribution the effective crack length is given by

$$a_{eff} = a_0 + r_p \tag{8}$$

For the PST crystals the onset of yielding depends strongly on the lamellar plane orientation with respect to the load direction, expressed by the inclination angle φ. For the PST the three angles φ = 0°, 45° and 90° correspond with the following yield strengths σ_Y = 400, 150, 600 MPa, respectively. These results are from compression tests [11] as well as from simulation based on the FE^2 method [12,13]. For comparison, the yield strength of the polycrystalline γTAB is σ_Y = 500 MPa.

The tests are conducted at ambient temperature and under quasi-static loading rates.

5.2 Interlamellar fracture of PST crystals (PST-IL)

Fig. 8(a) presents the experimental force-displacement curves (F-v_{LL}) for the PST with lamellar orientation perpendicular to the loading direction (respective principal stress component) with φ = 90°.

As a first step towards the cohesive parameter T_0 is varied (with $\Gamma_0 \to \infty$) as follows: T_0 = 1000 MPa as an upper and T_0 = 50 MPa as a lower bound estimate. The curve for T_0 = 50 MPa is close to experimental curves but underestimates the initial increasing loading range. The simulations have been carried out with the FE^2 method using the 3D homogenized periodic unit cell shown **in Fig. 5(b).**

The yield force, F_Y, can be determined by two options: a) for φ = 90° orientation the yield stress is σ_Y = 600 MPa and yield a (global) plane stress yield force F_Y = 688 MPa, b) for φ = 45° orientation the yield stress is σ_Y = 150 MPa and yields a plane stress yield force F_Y = 172 MPa, which is a plausible value in Fig. 8(a). The high yield strength, σ_Y, for φ =90° determined with the crystal plasticity model (FE^2) for a homogeneous crack free specimen, like the compression tests, is high as only hard slip modes prevail. However, if a crack is located in a lamellar colony, the softer slip mode (φ = 45°) is also activated and reduces the yield force, F_Y. The two cohesive parameters above show this effect.

In the present PST-IL the onset of fracture is still in the initial elastic slope, Fig. 8(a).

Fig. 8(b) presents an overview on the simulations with further variations: a) T_0 = 50 MPa with Γ_0 = 0.05, 0.1, 0.2 N/mm, b) T_0 = 100 MPa with Γ_0 = 0.05, 0.1 N/mm. All simulations are performed with the Quad-TSL.

Some important features can be emphasized. The F-v_{LL} curves from the simulations reach a distinct maximum force and continue by steep force decreasing. At maximum force (or next incrementel step beyond) crack initiation occurs sharply due to the break of the first cohesive element. Depending on the cohesive parameter combinations for T_0 and Γ_0, the simulations provide either a complete stable F-v_{LL} curve with stable crack extension or an unstable end immediately after the first cohesive element, which can be physically interpretated as unstable failure equivalent to what the bend specimens exhibit.

In the present case of PST-IL this transition depends on the T_0-values, i.e. T_0 = 50 MPa is still stable but T_0 = 100 MPa is already unstable. For increasing Γ_0 , however, the F-v_{LL} curves turn from unstable to stable. For a fixed Γ_0, the decreasing curve after crack initiation depends not on the T_0 parameter. In Fig. 8(b) the characteristic changes of the curves for increasing T_0 and Γ_0 are indicated.

As the F-v_{LL} curves are well below the yield point, interlamellar fracture of PST crystals are evidently not affected by global plasticity and can be described by linear-elastic fracture mechanics.

Therefore, in addition to the simulated curves in Fig. 8(b) some analytical F-v_{LL} curves for K_{Ic} = constant are included. The K_{Ic}-values are converted from the Γ_0-values as used in the simulations. The analytical function for a F-v_{LL} curve is valid for all a/W and decrease with increasing crack length for a constant K_{Ic} value. At the cross-point with the elastic slope the crack length ratio is a/W = 0.35.

For the same parameters (K_{Ic} or Γ_0) all analytical F-v_{LL} curves coincide perfectly with the simulated curves. However, the analytical curve does not contain a T_0 parameter as used in the simulation. The increasing part of the F-v_{LL} curves can be corrected by an effective crack length, a_{eff}, taking into account the plastic zone influence.

Fig. 8(c) shows the simulations with most appropriate cohesive parameters compared with the experimental F-v_{LL} curves. These results are in good agreement with the experimentally observed forces until unstable failure. The interlamellar fracture parameters for the binary PST crystal are: T_0 = 100 MPa, Γ_0 = 0.05 - 0.1 N/mm (equivalent to K_{Ic} = 3.1 - 4.4 MPa√m). The corresponding maximum separation is δ_0 = 0.6 - 1.1 μm.

From the experimental F-v_{LL} curves, the lowest force at crack initiation or unstable failure, respectively (specimens #1 and #3) is about 70 N and result in K_{Ic} = 3.5 MPa√m. The maximum force of the upper experimental curve (specimen #2) is not truly

relevant for interlamellar fracture as multiple cracks occurred after crack initiation (as will be seen in Fig. 9).

The experimental work of Yokoshima and Yamaguchi [26] for interlamellar fracture of the same binary PST crystal (Ti-49.3Al) provides a fracture toughness value of $K_{Ic} \approx 4.0$ MPa√m. Arata et al. [7] in cooperation with Chan et al. [27] found a crack inititiation range between 3 - 5 MPa√m for a binary TiAl alloy (Ti-47Al) in large colonies (≥ 600 μm).

Fig. 9(a) shows the broken bend specimens. In all specimens fracture occurred parallel to the lamellar boundaries. However, multiple cracks on two or three parallel planes also occurred. This phenomenon is due to a slight misalignment of the lamellar planes along the perfect crack plane as well as due to the weak interlamellar fracture process. The ligaments between the competing cracks might cause the irregular quasi-stable behaviour observed in the experiments. Only in one specimen (specimen #3) an almost single crack plane occurred throughout and yields the lowest fracture toughness above. It remains open, whether a perfect aligned lamellar boundary might occur and fractured with slightly less toughness as above.

Fig. 9(b) shows the interlamellar fracture surface. Some (white) spots remain from the α_2-phase. The lamellar γ-phases are not monolithic but are substructured in domains with many grain boundaries different slip system activations. All these very local details may contribute to the roughness of the fracture surface instead of a perfecly smooth plane.

5.3 Translamellar fracture of PST crystals (PST-TL)

Fig. 10(a,b) show the simulated and experimental F-v_{LL} curves for translamellar fracture of the binary PST crystal (PST-TL) under the inclination $\varphi = 0°$.

In Fig. 10(a) various cohesive tractions, T_0, in steps between 400 and 1000 MPa (with $\Gamma_0 \rightarrow \infty$) provide an appropriate value for T_0. The upper curve for the large value T_0 = 1000 MPa is equivalent to a pure elastic-plastic behaviour (as T_0 = 1000 MPa is beyond the needed stress-strain curve. The initial increasing part of the F-v_{LL} curve up to crack initiation is affected by T_0. Here, this part is best fitted by the limit curve for T_0 = 600 MPa, which is, therefore, a good approximation for the translamellar separation process.

The onset of plastic yielding expressed by the (global) plane stress yield force, F_Y = 458 N (for σ_Y = 400 MPa and $\varphi = 0°$), is below the experimental force at crack initiation and

maximum force. Hence, translamellar fracture occurs in a contained yielding regime. Similar to PST-IL the activation of different slip systems due to the presence of a crack may contribute to an early smooth nonlinear increase in the F-v_{LL} curve.

The estimated separation work, Γ_0, is presented in Fig. 10(b). For the fixed T_0 = 600 MPa, three values for Γ_0 are varried: Γ_0 = 5, 6 and 10 N/mm. A good approximation of the experimental F-v_{LL} curves is given for Γ_0 = 5 N/mm (with a maximum separation δ_0 = 9.5 μm). With this Γ_0, crack initiation is simulated very close to the observed experimental one as well as maximum force. However, the softening rate after maximum of force is larger than the measured experimental F-v_{LL} curves. This transition effect may be related to an increase of toughening durring crack extension (R-curve behaviour).

Analytical F-v_{LL} curves are included in Fig. 10(b) (denoted as a,b,c) with K_{Ic} converted from the Γ_0 values used in the simulations Here, the limitations of the analytical formulations based on K_{Ic}, can be clearly recognized. Here, global plasticity is involved. For K_{Ic} = 31.0 MPa√m (corresponding to Γ_0 = 5 N/mm) crack initiation is close to the experimental or simulated ones, provided small-scale yielding correction with a_{eff} is taken into account (curve A in Fig. 10(b)). Otherwise, the intersection point of the F-v_{LL} curves for K_{Ic} = constant with the elastic slope would significantly overestimate the experimental results. From the experimental curves, crack initiation yieldy J_i = 5.1 N/mm (equivalent to K_{Ic} = 31.3 MPa√m).

Fig. 11(a,b) illustrates the translamellar crack propagation process, shown by an in-situ SEM image taken from the side-surface of a bend specimen. In Fig. 11(a) γ-domains and an α_2-phase can be seen (the α_2 line is due to lamellar planes slighly inclined to the surface plane). A vertical section (A-B) was machined through the specimen to observe thickness effects on translamellar fracture. Fig. 11(b) shows the formation of massive local plastic deformation in a soft oriented γ-domain, as indicated by the slip traces accompanied by some advancing microcrack ahead the main crack. However, no significant microcraking with shear ligaments adjacent to the propagating crack were observed. The PST kernels in the bend specimen are prepared such, that the slip direction $\langle\bar{1}10\rangle$ is perpendicular to the crack plane. Further information about the translamellar orientations is given in [26].

Fig. 12(a,b) shows the section A-B (indicated in Fig. 11(a)) across the thickness just behind the crack front after the test. Across the thickness, many delaminations can be identified, which were classified here in three typical length scales (I, II, III). The largest series of delamination type I have a length of more than 250 μm and a periodic

distance of approximately 200 μm. The delamination type II has a length of approximately 40 μm and a distance of approximately 30 μm. The smallest delamination type III has a length of less than 10 μm and can be found between almost all lamellae. The mean thicknes of the γ-lamellae is about 2 μm.

Fig. 12(b) enlarges the local situation. Large plastic lamellar necking causes the vertical interlamellar delaminations and develop arbitrarily along α_2/γ or γ/γ interfaces. The corresponding translamellar fracture surface is shown in Fig. 13(a-d). Each γ-lamella failed by cleavage fracture depending on the orientation of the crystallographic {111} planes in the γ -phase, either for the γ -matrix or γ -twin lamellae. Due to the numerous delaminations, the global fracture surface is very rough, Fig. 13(b).

The delaminations occur due to the extended interface planes with weak interlamellar fracture toughness (see PST-IL). Local plastic necking produces transverse stresses, which are high enough to initiate the parallel delaminations. This effect may responsible for the descending part of the F-v_{LL} curve (Fig. 10(b)), which is lower than the simulated curve with $\Gamma_0 = 5$ N/mm as no (vertical) delaminations are taken into account.

In Fig. 10(b) an increase of resisance during crack extension due to delamination can be explained by an increase of toughness from $\Gamma_0 = 5$ to 6 N/mm. The delamination effect could be simulated, if separate cohesive interfaces in the (vertical) lamellae would be introduced provided with a fracture toughness from the interlamellar PST fracture (PST-IL: $T_0 = 100$ MPa, $\Gamma_0 = 0.1$ N/mm). However, such refined modelling is beyond the scope of this investigation.

5.4 Fracture of TiAl polycrystal

Results for the polycrystalline γTiAl (specific composition denoted as γTAB) will be presented for bend specimens with fracture planes in translamellar (TD) and longitudinal (LD) directions (Fig. 4). Tensile tests are done for TD fracture only.

Fig. 14(a,b) schematically illustrates both sides, the real polycrystalline microcrostructure with a zigzag fracture topology and the idealization made for the simulations. Irrespective of the colonies with their different lamellar orientations, the cohesive model applies homogenized meanfield parameters acting on a perfect plane. Any roughness effects from the real fracture surface are included in such cohesive parameters.

Stress-strain curves for γTAB are determined from tensile tests with a square section of

2x2 mm^2 oriented for TD fracture and are shown in Fig. 15. The elastic modulus is E = 175000 MPa and is equal to that of the PST crystal. The tensile strength can be used as the homogeneous cohesive traction, T_0, which has a mean value of T_0 = 780 MPa. A true stress-strain curve is fitted for the FE input. Although the total strain at failure is only about 1.5% the nonlinear part of the stress-strain curve has an important effect in the simulation and should not be neglected.

Fig. 16(a) shows all experimental force-crack mouth opening displacement curves (*F-CMOD*) for a/W = 0.6 with TD and LD fracture, while Fig. 16(b) shows the curves for a/W = 0.35 and TD fracture only.

Fracture in translamellar direction (TD)

In a first step limit curves are determined for various cohesive tractions, T_0 = 300, 400, 500 and 780 MPa, each with $\Gamma_0 \to \infty$ (Fig. 16(ab)). 2D plane strain conditions are applied in the simulations. The appropriate cohesive traction, T_0, is in the range of T_0 = 500 - 780 MPa. The other two curves are softer than the initial increasing part of the experimental *F-CMOD* curves.

The lower bound plane stress yield force, F_Y, is above the maximum force of the experiments. Thus it can be assumed that nearly quasi-brittle fracture prevails. All experimental curves for a/W = 0.35 (Fig. 16(a)) failed unstably at maximum force or slightly beyond. The physical crack initiation was not experimentally determined, but it seems near before the maximum force. For a/W = 0.6 (Fig. 16(b)) the experimental curves are stable far beyond the maximum and exhibits a stable jump with subsequent crack arrest and further stable crack extension.

In a second step the cohesive work, Γ_0, was varied as Γ_0 = 2.5, 3, 4 and 5 N/mm, while T_0 was fixed at 780 MPa as the most relevant value from the tensile tests (Fig. 15). It should be emphasized that for the Quad-TSL stable crack extension as well as unstable failure can be simulated, depending on the cohesive parameter combination T_0 versus Γ_0. For Γ_0 = 2.5 and 3 N/mm unstable failure occurred, while for $\Gamma_0 \geq 4$ N/mm only stable *F-CMOD* curves are obtained. This quantitative effect belongs to T_0 = 780 MPa. If T_0 is changed (for example T_0 higher than 780 MPa) only unstable failure would be predicted, while for reduced T_0 (lower than 780 MPa) only stable curves would be obtained.

For the determined parameter combinations, unstable failure occurs just after removing the first cohesive element. The cohesive elements and the corresponding nodes of the solids aside have a distance of 15 µm. The stable *F-CMOD* curves initiate at the sharp

maximum force, followed by force decreasing during increasing *CMOD*.

Furthermore, the question about the appropriate shape of the cohesive TSL is recalled, i.e. the two limiting shapes for the traction-separation law, the Quad-TSL and Tria-TSL, are compared in Fig. 17(a). The included *F-CMOD* cuves from the Tria-TSL differ significantly from thoese of the Quad-TSL. Firstly, no unstable failure is obtained for all T_0 and Γ_0 variations and combinations. Secondly. crack initiation occurs far beyond maximum force, which is physically not correct. At maximum force these curves are smoothly rounded. This pronounced effect, as compared to Quad-TSL, results from the much longer and flatter softening part of the Tria-TSL, which allows smooth incremental reduction of the cohesive traction down to zero. It is interesting that the descending parts of the curves for both TSL types coincide. From these results it can be concluded that only the Quad-TSL in Fig. 17(a) is appropriate for simulating quasi-brittle fracture.

In Fig. 17(b) further variations are shown. Here, the *F-CMOD* curves for T_0 = 500 MPa are compared with those for T_0 = 780 MPa, both for Γ_0 = 2.5, 5, and the limit ∞, to see how sensitive the T_0-variation might be. The deviation among the curves with both T_0-values is pronounced. It should be emphasized that the descending parts of the *F-CMOD* curves (beyond force maximum) coincide for the same cohesive work parameter, Γ_0, irrespective of T_0. Moreover, for T_0 = 500 MPa no unstable failure is obtained in the simulations, but should occur for $\Gamma_0 \leq 2$ N/mm.

For completion, the analytical *F-CMOD* curves for K_{Ic} = constant are included in Fig. 17(b). K_{Ic}-values are again from the Γ_0 values. These analytical curves coincide perfectly for the descending parts of the curves. The elastic compliance for the increasing force has to be corrected by an effective crack length, a_{eff} (as is already shown in Fig. 10 for the PST-TL).

The behaviour of the *F-CMOD* curves as presented in Fig. 17(a,b) for a/W = 0.6 is also valid for a/W = 0.35, including the unstable-to-stable transition effects as well as the effects of the Tria-TSL.

The final situation of simulations versus experiments for TD fracture is condensed in Fig. 18(a,b) for a/W = 0.6 and 0.35. The cohesive parameters must of course be equal for both a/W which are: T_0 = 780 MPa, Γ_0 = 3 N/mm for unstable failure and Γ_0 = 4 N/mm for stable crack extension. The maximum force prediction matches well with the experimental scatter band. However, the descending part of the simulated *F-CMOD* curve does not satisfy the characteristic of the experimental curves. In particular for a/W = 0.35 all experimental curves are rounded when approaching the maximum force level.

This behaviour was similarly observed for the PST-TL (Fig. 10(b)). Some steps of crack extension (a_1, a_2, a_3) are indicated in Fig. 18(a,b) to express the high sensitivity of the force even for a small microstructural related fracture spot. The experimental scatter band results probably from stochastical variations.

Fracture in longitundal direction (LD)

In Fig. 16(a) the experimental curves for LD fracture were shown and compared with the curves for TD fracture. The maximum force for LD fracture is about 66% less than that for TD fracture.

The simulations with the appropriate cohesive parameters for LD fracture are shown in Fig. 19(a,b) for various limit curves, i.e. T_0 in the range between 300 to 780 MPa and with $\Gamma_0 \rightarrow \infty$. The decreasing part of the *F-CMOD* curves for Γ_0 = 1.3 N/mm is equal for both, T_0 = 300 and T_0 = 400 MPa, and coincides with the respective analytical curve for K_{Ic} = 15.2 MPa√m.

The final situation is condensed in Fig. 19(b), where the experimental scatter band is compared with the simulation for T_0 = 400 MPa and Γ_0 = 1.2 N/mm. Again (as for TD fracture before) the experimental curves exhibit a smooth curvature at maximum force. All experimental curves exhibit this typical behaviour. In contrast, the simulations predict a steep decrease of the force just after crack initiation if only one cohesive element is removed. Three further crack extension steps (a_1 a_2, a_3) are indicated in Fig. 19(b) to demonstrate how sensitively crack extension reduces the force.

If, for example, the descending part of the simulated curves would be improved by stepwise increasing Γ_0, the complete experimentel curve could be better approximated. A smooth transion of Γ_0 is related to an increasing resistance during stable crack extension.

The cohesive traction, T_0 = 400 MPa for LD fracture, is much less than T_0 = 780 MPa for TD fracture and is even less than the yield strength σ_Y = 500 MPa from a tensile test with TD fracture (Fig. 15). This means, that the stress-strain curve for LD fracture would fail at very small plastic strains. Unfortunately, no tensile tests for LD fracture could be taken from the small diameter of the γTAB bar (Fig. 4) to prove independently the value T_0 = 400 MPa.

The fractures surfaces for TD and LD fracture of γTAB are compared in Fig. 20(a-d). In Fig. 20(a,b) a cutout ahead of the starter notch presents the different fracture topologies. The fracture surfaces are relatively rough and cragged. In Fig. 20(a) the lamellar colonies are almost randomly distributed. In Fig. 20(b) the fracture surface in the

colonies is aligned in LD, which is a result of the extrusion process.

A detailed view on the microstructure of the fracture surface is shown for TD in Fig. 20(c) and Fig. 20(d) for LD fracture. The LD fracture surface contains interlamellar fractured colonies, which reduce the global fracture toughness as observed in the *F-CMOD* curves for LD. This sporadically distributed interlamellar fracture does not cause unstable fracture. Obviously, the growing crack does not jump in a larger extend to the weak interlamellar fracture planes, at least not in fine-grained lamellar γTiAl.

The following Tab. 1 summarises the relevant parameters for the investigated materials and fracture modes.

Material-Fracture type	σ_Y	T_0	Γ_0	δ_0	K_{Ic}
	MPa	MPa	N/mm	µm	MPa√m
PST-IL	150-600	100	0.05-0.1	0.6-1.1	3.1-4.4
PST-TL	400	600	5-6	9.5-11.4	31-34
Poly-TD	500	780	3-4	4.4-5.9	24-34
Poly-LD	400	400	1.2	3.7	15

Tab. 1

6. Discussion

The results of the simulation confirm the performance of the cohesive model for quasi-brittle fracture, both for stable behaviour with crack extension and for unstable fracture. This can be assured by proper determination of the cohesive parameters, T_0 and Γ_0, as they reflect the sensitivity of the material behaviour. The determination of the cohesive parameters can be well performed by simulations for which only experimental records like force-displacement are necessary. T_0 is pronounced in the initial increasing part of such curves, while Γ_0 reflects the descending part due to stable crack extension.

The cohesive model is applied very locally in the FE mesh, where the parameters T_0 and Γ_0 are assumed to be constant for crack front propagation. Global plasticity is contained in solid elements outside the physical fracture process. Thus, no increases of the fracture resitance is considered.

The cohesive parameters can be taken from simulations which are fitted to experimentally measured (global) responses.

Moreover, for low ductility with quasi-brittle failure, the tensile strength can be taken directly as the cohesive traction, T_0. The physical crack initiation, determined either in terms of the *J*-Integral or K_{Ic}, can be used as the separation work, Γ_0. The use of K_{Ic} is valid only within the linear behaviour of a force-displacement curve. Under these conditions, the simulated force-displacement curves coincide with the analytical formulation for elastic material behaviour using K_{Ic} = constant as the fracture criterion.

The applied 2D plane strain boundary conditions in the simulations (here applied for the polycrystal) is obviously not sufficient enough to describe the experimental curves in their whole range. The 2D simulations are conservative estimations. Stochastic effects across the thickness cannot be considered. However, the development of a continuouse crack front is a genuine 3D progress with many microstructural facets across the different oriented lamellae and might contribute to the observed increasing fracture toughness beyond initial crack initiation.

An other relevant aspect for the polycrystal simulation comes from the activation of the different crystal slip systems around a crack tip as compared to the von Mises flow rule (with σ_Y = 500 MPa). It may assumed, that the soft slip system ($\varphi = 45°$ with lower σ_Y) will be activated in an early stage. The local plasticity effects may contribute to an increasing fracture toughness effect. Furthermore, twinning in the γ-lamellae may have a considerable contribution to fracture toughness as reported earlier by Dève and Evans [28].

Delaminations can easily occur along lamellar planes (α_2/γ, γ/γ with Γ_0 = 0.1 N/mm or K_{Ic} = 3-4 MPa$\sqrt{m}$). For the PST-TL this weak effect is clearly demonstrated. The large delaminations can be fully developed only for certain lamellar plane orientation, $\varphi = 0°$. Many of such parallel delaminations help to enhance fracture toughness.

It should be noted, that a further translamellar oriented crack with $\varphi = 0°$ is not considered, where the crack front is located perpendicular and parallel to the lamellar planes. However, immediately after crack initiation the main crack deviates into the (vertial) weak lamellar planes similar to PST-IL:

Fracture toughness of the extruded γTAB is considerably different for transverse (TD) and longitudinal (LD) directions. This can be explained by the dominating alignment of the lamellar planes in LD, introduced by the extrusion process, which reduces fracture toughness due to the contribution of interlamellar fracture.

For the fine-grained polycrystalline γTAB only very few delaminations could be found lying parallel to the acting force (principal stress). The different lamellar inclinations do

not allow some zigzag delaminations, although in each colony transverse stresses are acting. Obviously the stiffness of all neighbour colonies is responsible for the absence of delaminations.

From the few experimental curves for TD fracture a TD crack did not completely deflect to the weaker longitudinal lamellar planes. This would be worth for a component with more arbitrary geometry and loading. It should be noted, that the cohesive model could also be applied for a defect (crack) free component.

For various fully-lamellar polycrystals, Chan and Kim [5] have investigated the influence of the lamellar microstructure on fracture toughness. These results belong to a large colony size (≥ 500 μm). From bend specimens, still in the global elastic regime, they found an R-curve effect, i.e. increasing fracture toughness from initiation (K_{Ic} ≈ 16 MPa√m) up to saturation of about 25-30 MPa√m. This increase is confined within small crack extension, less than 200 μm, i.e. only within a colony. The R-curve effect is correlated with the proposed accumulated shear ligament model. However, for fine-grained fully lamellar microstructure of about 150 μm mean size of the colonies, the R-curve effect is continuously reduced and the corresponding crack extension is detected within100 μm only [29]. The R-curve increases from 16 to 22 MPa√m. From these results, it can be argued, that an R-curve effect for fine-grained polycrystals might exists but remains small.

An fracture toughness increase for γTAB can also be estimated from the *F-CMOD* curves, when the simulated curves are fitted to the experimental ones. Crack initiation for TD fracture in γTAB occurs at Γ_0 ≈ 2.5-3 N/mm (K_{Ic} ≈ 22-24 MPa√m) and increases at about 400 μm crack extension to Γ_0 = 4-5 N/mm (K_{Ic} = 28-31 MPa√m).

A considerable improvement of the simulation can be expected by a full 3D modelling with small cohesive elements (of about 10-20 μm in the order as δ_0) in combination with a stochastic concept, in which a variation of the cohesive parameters, T_0 and Γ_0, are randomly distributed over the fracture plane. First results of an investigation of Kabir et al. [30], as well done for γTAB, show an improvement of the predictions with respect to the experimental scatter with unstable fracture or pop-in events.

The microstructural parameters, like lamellar thickness, spacing, colony size as well as their 3D orientation are not considered in the phenomenological cohesive model. Hence, any change of microstructural lengths need individual experiments.

The cohesive parameters are acting on a representative microstructural volume element (RVE). The values of the cohesive parameters indirectly depend on the characteristics

of such an individual microstructural RVE. Especially the separation, δ_0, should have a characteristic relationship to the microstructure. In contrast to the single fracture parameters (J-Integral, K_{Ic}) the separation of a RVE at the point of fracture is δ_0, which is related to T_0 and Γ_0 (equ. (3)). Fig. 21(a,b,c) shows schematically RVEs for three typical lamellar orientations: $\varphi = 0°$, 45° and 90°. For the investigated materials it was found as follows in Tab. 2.

Material-Fracture type	K_{Ic}	T_0	Γ_0	δ_0	Lamellar thickness L_S of γ	φ	RVE height L_R	δ_0/L_R
	MPa√m	MPa	N/mm	µm	µm	°	µm	-
PST-IL	3.1-4.4	50-100	0.05-0.1	0.6-1.1	2.1	90	$\approx 0.2L_S$	≈ 2
PST-TL	31-34	600	5-6	9.5-11.4	2.1	0	$\approx 2\text{-}3L_S$	≈ 2
Poly-TD	24-28	780	3-4	4.4-5.9	0.7	30*)	$\approx 3L_S*2/\sqrt{3}$	≈ 2

*) mean for random orientation

Tab. 2

If we use the lamellar thickness, L_S, and make some assumptions about the RVE size in relation to the lamellae one can estimate a characteristic length scale based on the cohesive separation δ_0, which depends on T_0 and Γ_0.

7. Conclusions

Two materials are investigated, the binary PST crystal (Ti-49.3Al) and a γTiAl polycrystal γTAB (Ti-47Al-3.7(Nb,Cr,Mn,Si)-0.5B), both with respect to the fracture toughness of different crack plane orientations. The main conclusions reached in this study are as follows.

1. The cohesive model has been successfully validated for quasi-brittle materials like γTiAl. The necessary link is the determination of the cohesive parameters, which have been identified by simulations of experimentally measured force-displacement curves of precracked bend specimens.
2. The cohesive model predicts crack initiation, followed either by stable crack extension or unstable failure depending on the cohesive parameter. The occurrence of the last both is sensitively triggered by the parameters and is in accordance with experimental evidence.

3. The identified cohesive parameters by simulations agrees well with experimental results for crack initiation. Microstructural changes are ref˝lected sensitively by the cohesive parameters.

4. Interlamellar fracture toughness of PST crystals (PST-IL) is very brittle with K_{Ic} = 3-4 at the most. PST crystals with lamellar planes oriented parallel to the force direction (PST-TL) exhibits extended delaminations as interlamellar fracture (PST-IL). Transverse crack initiation is about K_{Ic} = 30 MPa√m.

5. In the extruded polycrystal fracture toughness depends on the crack plane orientation with respect to the applied force. This effect results from the extrusion process that preferentially induces lamellar colonies parallel to the extrusion direction. All weak colony arrangement reduces the maximum attainable force.

6. The maximum separation at fracture, δ_0, depending on the traction, T_0, and separation work, Γ_0, can be regarded as a characteristic length with respect to a representative microstructural volume.

Acknowledgments

The financial support of this work by the German Science Foundation (DFG) within the Collaborative Research Centre SFB 371 "Micromechanics of Multiphase Materials" is gratefully acknowledged. The authors wish to thank Arno Bartels and Henning Uhlenhut (Technical University of Hamburg-Harburg) for providing the PST crystal and cooperation. The authors thank their colleagues at GKSS, Fritz Appel, Uwe Lorenz, Michael Oehring, and Jonathan Paul for providing the material γTAB, their general support and helpful discussions. Ingo Scheider at GKSS is kindly acknowledged for his support in applying the cohesive model.

References

[1] Appel F, Wagner R. Microstructure and deformation of two-phase γ-titanium aluminides. Mater Sci Eng Reports 1998;R22:187-268.

[2] Chan KS. Micromechanics of shear ligament toughening. Metall Mater Trans A 1991;22A:2021–2029.

[3] Chan KS. Understanding fracture toughness in gamma TiAl. JOM - Technical Journal of The Minerals, Metals & Material Society (TMS) 1992;44:30–38.

[4] Chan KS. Toughening mechanisms in titanium aluminides. Metall Mater Trans A 1993; 24A: 569–583.

[5] Chan KS, Kim Y-W. Effects on lamellae spacing and colony size on the fracture resistance of a fully-lamellar TiAl alloy. Acta metall mater 1995;43:439-451.

[6] Arata JJM, A. Needleman A, K.S. Kumar KS, and W.A. Curtin WA. Microcrack nucleation and growth in elastic lamellar solids. Int J Fract 2000;105:321–342.

[7] Arata JJM, Kumar KS, Curtin WA, Needleman A. Crack growth in lamellar titanium aluminide. Int J Fract 2001;111:163–189.

[8] Arata JJM, Kumar KS, Curtin WA, Needleman A. Crack growth across colony boundaries in binary lamellar TiAl. Mater Sci Engng A 2002;329-331:532–537.

[9] Inui H, Toda Y, Yamaguchi M. Plastic deformation of single crystal of a $D0_{19}$ compound with an off-stoichiometric composition (Ti-36.5 at.% Al) at room temperature. Phil Mag A 1993;67:1315–1332.

[10] Lebensohn R, Uhlenhut H, Hartig C, and Mecking H. Plastic flow of γ-TiAl-based polysynthetically twinned crystals: micromechanical modeling and experimental validation. Acta mater 1998;46:4701–4709.

[11] Uhlenhut H. Ursachen plastischer Anisotropie von γ-TiAl-Basislegierungen. PhD thesis, Technical University Hamburg-Harburg, 1999.

[12] Werwer M, Cornec A. Numerical simulation of plastic deformation and fracture in polysynthetically twinned (PST) crystals of TiAl. Comp Mater Sci 2000; 19:97–107.

[13] Cornec A, Werwer M, Heitmann V. Micromechanical modeling of deformation and fracture in lamellar gamma TiAl alloys. In: Kim Y-W, Clemens H, Rosenberger A. (Eds.). Gamma Titanium Aluminides 2003. The Minerals, Metals & Materials Society (TMS); 2003, p. 493-501.

[14] Werwer M. Mikromechanische Modellierung des Verformungs- und Bruchverhaltens von lamellarem TiAl. PhD thesis, Technical University Hamburg-Harburg, 2005.

[15] Werwer M, Cornec A. The role of superdislocations for the plastic deformation of lamellar TiAl. Accepted for publication in Int. J. Plasticity.

[16] Feyel F, Chaboche J-L. FE^2 multiscale approach for modelling the elastoviscoplastic behaviour of long fibre SiC/Ti composite materials. Computer Methods in Appl Math and Engng 2000;183:309–330.

[17] Asaro RJ. Crystal plasticity. J Appl Mech 1983;50:921–934.

[18] ABAQUS 6.4, ABQUS Inc., Providence, RI, USA (2003).

[19] Scheider I. Bruchmechanische Bewertung von Laserschweißverbindungen durch numerische Rißfortschrittsimulation mit dem Kohäsivzonenmodell. PhD Thesis, Technical University Hamburg-Harburg, 2001.

[20] Scheider I. Simulation of cup-cone fracture in round bars using the cohesive zone model. In: First MIT Conference on Computational Fluid and Solid Mechanics. Vol. 1. Amsterdam: Elsevier; 2001. p. 460-462.

[21] Scheider I, Brocks W, Simulation of cup-cone fracture using the cohesive model. Eng Fract Mech 2003;70:1943-1961.

[22] Cornec A, Scheider I, Schwalbe K-H, On the practical application of the cohesive model, Eng Fract Mech 2003;70:1963-1987.

[23] Loi FT, Li H. Numerical simulation of quasi-brittle fracture processes using the discrete cohesive crack model, Int J Mech Sci 2000;42:367-397.

[24] Tada H, Paris PC, Irwin GR. The stress analysis of cracks handbook. Third Edition, ASME Press, New York: American Society of Mechanical Engineers, London: Professional Engineering Publishing Ltd; 2000.

[25] Murakami Y et al. Stress intensity factors handbook. Kyoto: The Society of Materials Science, Japan; Oxford: Elsevier Science Ltd; 2001.

[26] Yokoshima S, Yamaguchi M. Fracture behavior and toughness of PST crystals of TiAl. Acta mater 1996;44:873–883.

[27] Chan KS, Onstott J, Kumar S. The fracture resistance of a binary TiAl alloy. Metall Mater Trans A 1993; 31A:71-80.

[28] Dève HE, Evans AG. Twin toughening in titanium aluminide. Acta metall mater 1991;39:1171-1176.

[29] Chan KS, Donald SS. Fatigue and fracture behavior of a fine-grained lamellar TiAl alloy. Metall Mater Trans A 1997;28A:79-90.

[30] Kabir R, Cornec A, Brocks W. Simulation of quasi-brittle fracture of lamellar γTiAl using the cohesive model and a stochastic approach. Comp Mat Sci 2006 (in press).

Figure Captions

Fig. 1 Crystallographic structures of γ-based TiAl: (a) D019 structure of α_2-phase (Ti_3Al); (b) L10 structure of the γ-phase (TiAl).

Fig. 2 Microstructure of γ-based TiAl: (a) Lamellar substructure of γTiAl consisting of α_2-, γ-matrix and γ-twin lamellae; (b) morphological slip modes in lamellar γTiAl for determining crystal plasticity parameters.

Fig. 3 PST test specimen: dimensions of the three-point bend specimen and the PST kernels for translamellar and interlamellar fracture.

Fig. 4 Polycrystal test specimens: (a) radial and longitudinal section through the γTAB rod; (b) specimen from the γTAB rod; (c) transverse (TD) and longitudinal (LD) fracture orientation; (d) flat bar tensile specimen; (e) bend bar specimen dimensions with spark eroded notch.

Fig. 5 Periodic unit cell: (a) realistic lamellar substructure, (b) simplified model.

Fig. 6 Cohesive model background: (a) damage process ahead of a crack-tip (taken from the surface of a PST crystal); (b) its macroscopical representation by the cohesive model.

Fig. 7 Traction-separation-laws (TSL): (a) quadratic TSL (Quad-TSL); (b) triangular TSL (Tria-TSL).

Fig. 8 Determination of cohesive parameters for interlamellar PST fracture (PST-IL): (a) estimation of T_0 from numerical limit curves ($\Gamma_0 \rightarrow \infty$) compared with experimental curves; (b) variation of cohesive cohesive parameters T_0 and Γ_0; (c) final comparison of simulation and experiment.

Fig. 9 Translamellar fracture (PST-IL): (a) surface view of bend specimens; (b) fracture surface topology.

Fig. 10 Determination of cohesive parameters for translamellar PST fracture (PST-TL): (a) estimation of T_0 from numerical limit curves ($\Gamma_0 \rightarrow \infty$) compared with experimental curves; (b) fracture related variation of cohesive cohesive parameters T_0 and Γ_0 compared with experimental curves.

Fig. 11 Translamellar PST fracture (PST-TL) from in-situ observations: macro-crack development (cut A-B is shown in Fig. 12), (b) near crack tip slip deformation in a domain (different from Fig. 11(a)).

Fig. 12 Translamellar PST fracture (PST-TL): (a) cut A-B from Fig. 11 across the thickness; (b) detail of the translamellar fracture with delaminations.

Table Captions

Tab. 1: Relevant material for the investigated materials: yield strength, cohesive parameters, classical fracture toughness.

Tab. 2: Characteristic relations of the microstructures of the investigated materials.

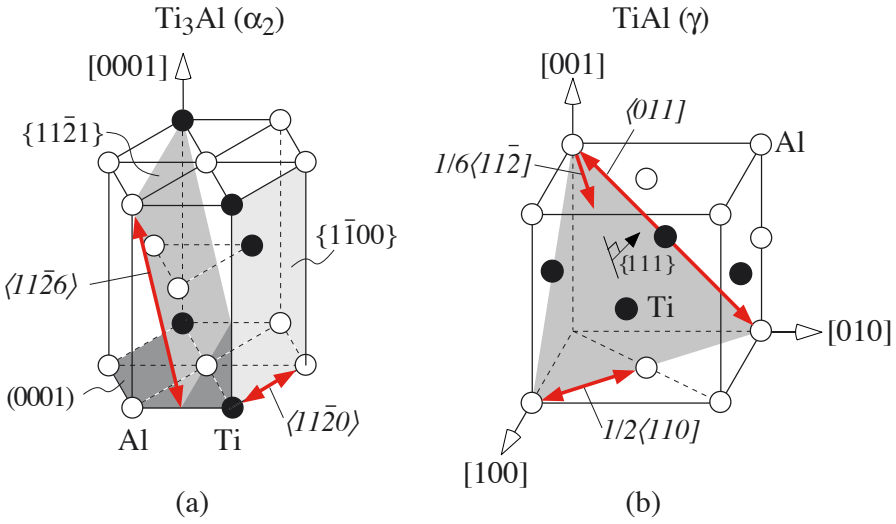
Ti3Al (α2)
[0001]
{11$\bar{2}$1}
{1$\bar{1}$00}
⟨11$\bar{2}$6⟩
(0001)
Al
Ti
⟨11$\bar{2}$0⟩
(a)
TiAl (γ)
[001]
⟨011]
Al
1/6⟨11$\bar{2}$]
{111}
Ti
[010]
1/2⟨110]
[100]
(b)

Fig. 1

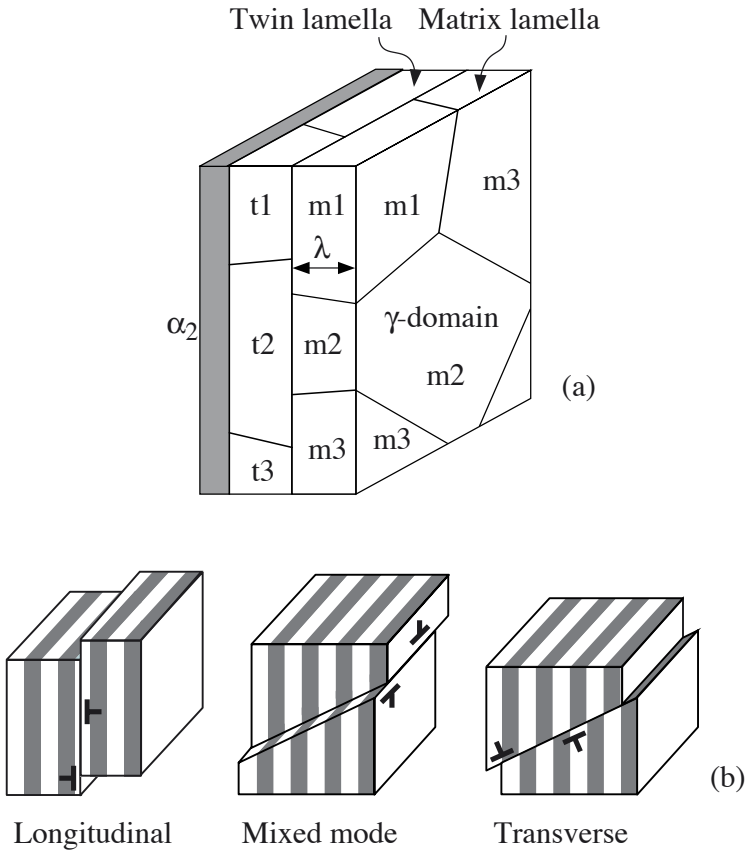
Twin lamella
Matrix lamella
t1
m1
m1
m3
λ
α2
t2
m2
γ-domain
m2
(a)
m3
m3
t3
Longitudinal
Mixed mode
Transverse
(b)

Fig. 2

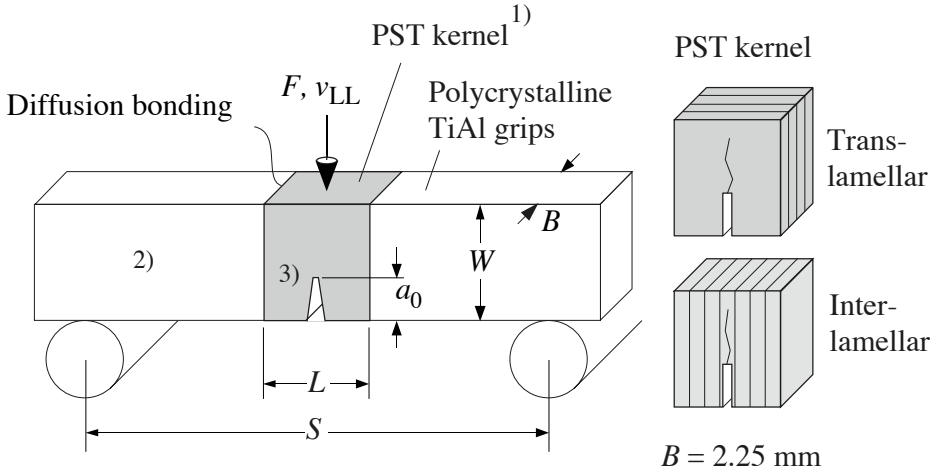

1) PST binary crystal: Ti-49.3Al (at%)
2) Bending arms from aγTiAl polycrystal
3) Spark erroded notch 0.06-0.07 mm

Fig. 3

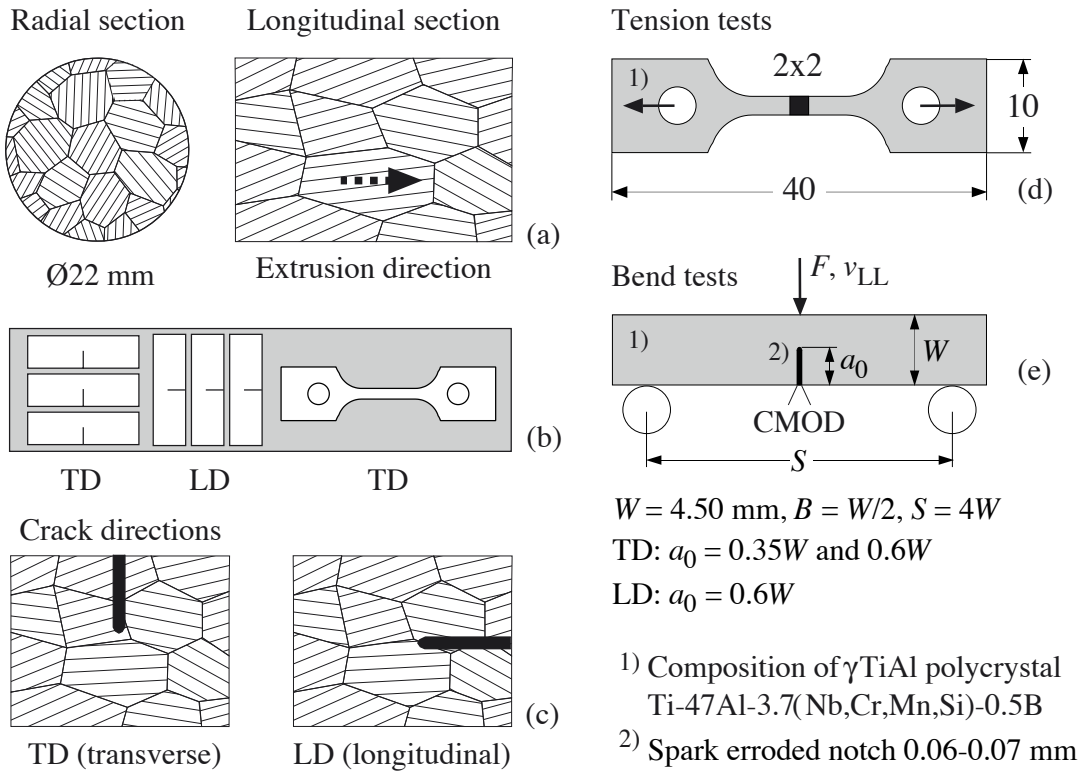

$W = 4.50$ mm, $B = W/2$, $S = 4W$

TD: $a_0 = 0.35W$ and $0.6W$

LD: $a_0 = 0.6W$

[1] Composition of γTiAl polycrystal Ti-47Al-3.7(Nb,Cr,Mn,Si)-0.5B

[2] Spark erroded notch 0.06-0.07 mm

Fig. 4

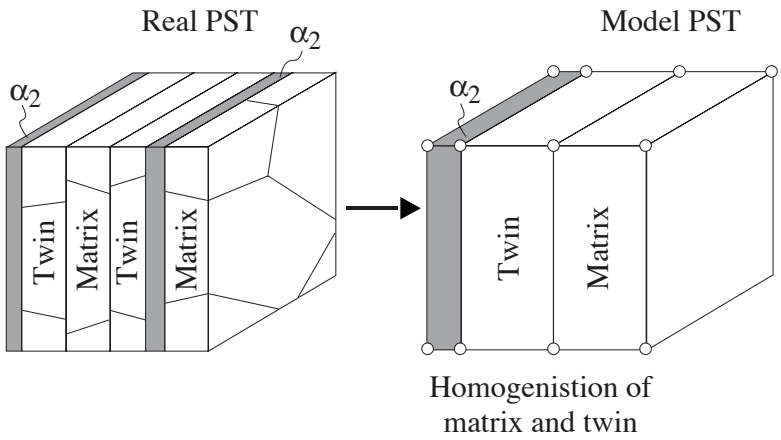
Real PST
Model PST
α2
α2
α2
Twin
Matrix
Twin
Matrix
Twin
Matrix
Homogenistion of
matrix and twin
(a)
(b)

Fig. 5

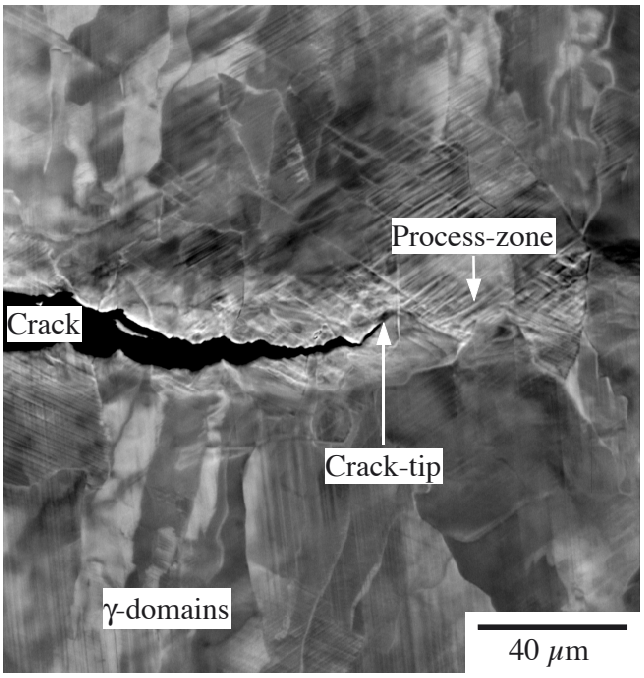
Process-zone
Crack
Crack-tip
γ-domains
40 μm

(a)

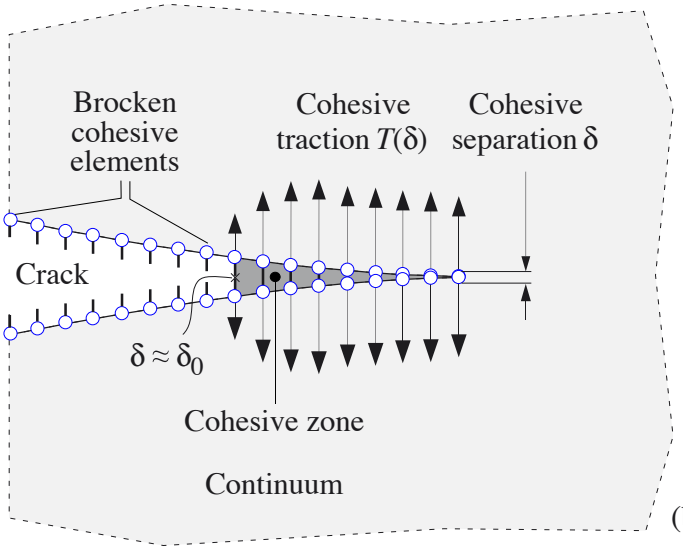
Brocken cohesive elements
Cohesive traction T(δ)
Cohesive separation δ
Crack
δ ≈ δ0
Cohesive zone
Continuum

(b)

Fig. 6

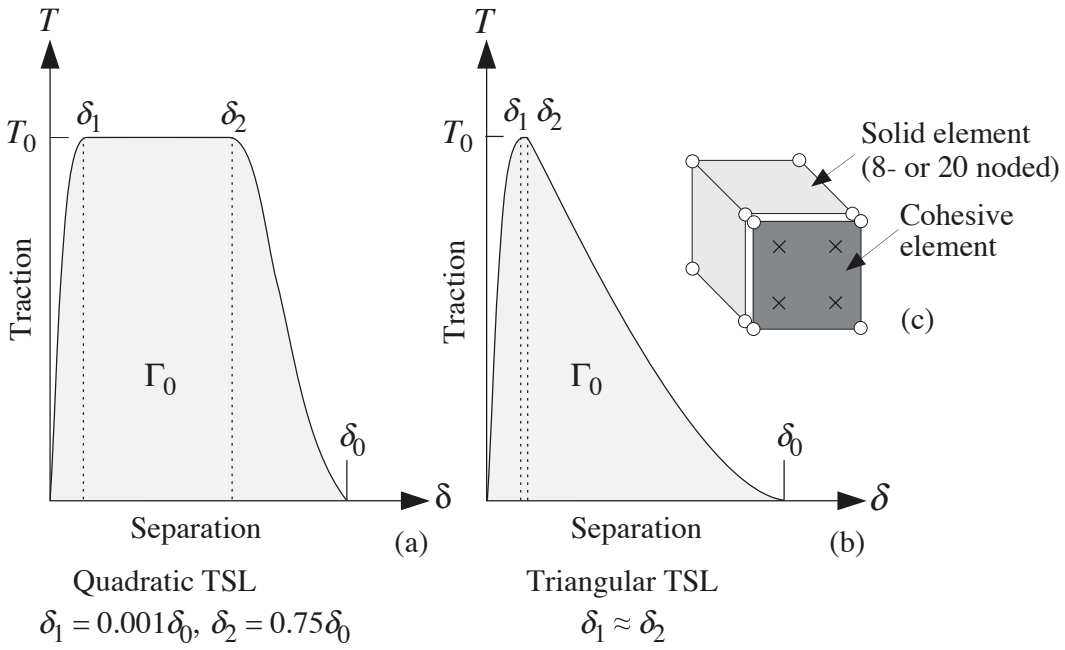
T
T0
δ1
δ2
Traction
Γ0
δ0
δ
Separation
(a)
Quadratic TSL
δ1 = 0.001δ0, δ2 = 0.75δ0
T
T0
δ1 δ2
Traction
Γ0
δ0
δ
Separation
(b)
Triangular TSL
δ1 ≈ δ2
Solid element
(8- or 20 noded)
Cohesive
element
(c)

Fig. 7

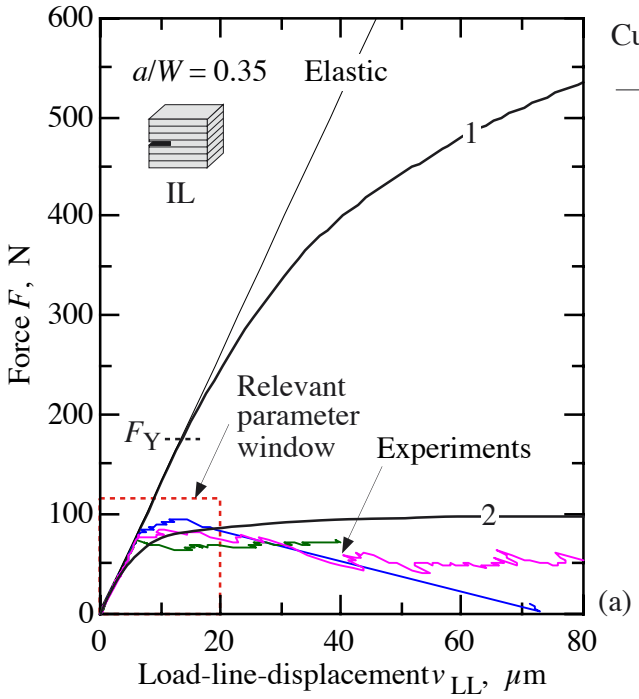

Curve	T_0 MPa	Γ_0 N/mm
1	1000	∞
2	50	∞

Fig. 8a

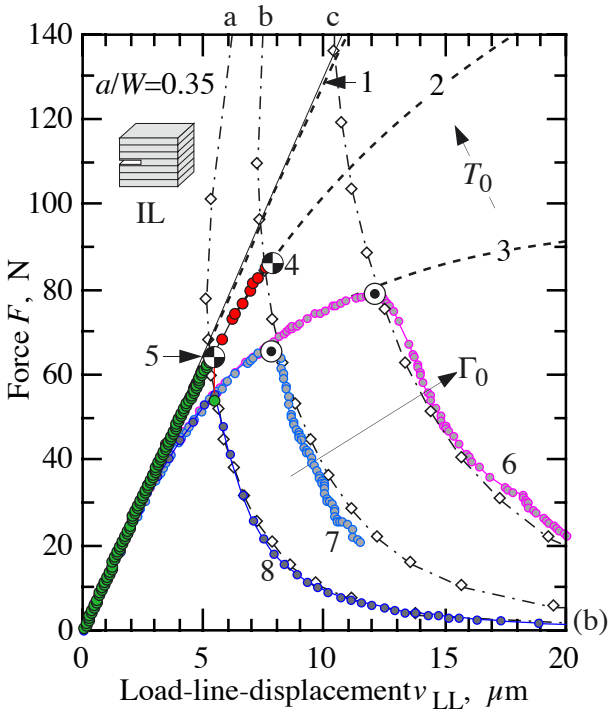

Curve	T_0 MPa	Γ_0 N/mm	δ_0 μm
1	1000	∞	∞
2	100	∞	∞
3	50	∞	∞
4	100	0.10	1.1
5	100	0.05	0.6
6	50	0.20	4.5
7	50	0.10	2.3
8	50	0.05	1.1

Curve	K_{Ic} MPa√m	Γ_0 N/mm
a	3.1	0.05
b	4.4	0.10
c	6.2	0.20

a,b,c: Curves for K_{Ic} = constant

⦿ Iniation followed by stable crack extension

◒ Unstable failure

Fig. 8b

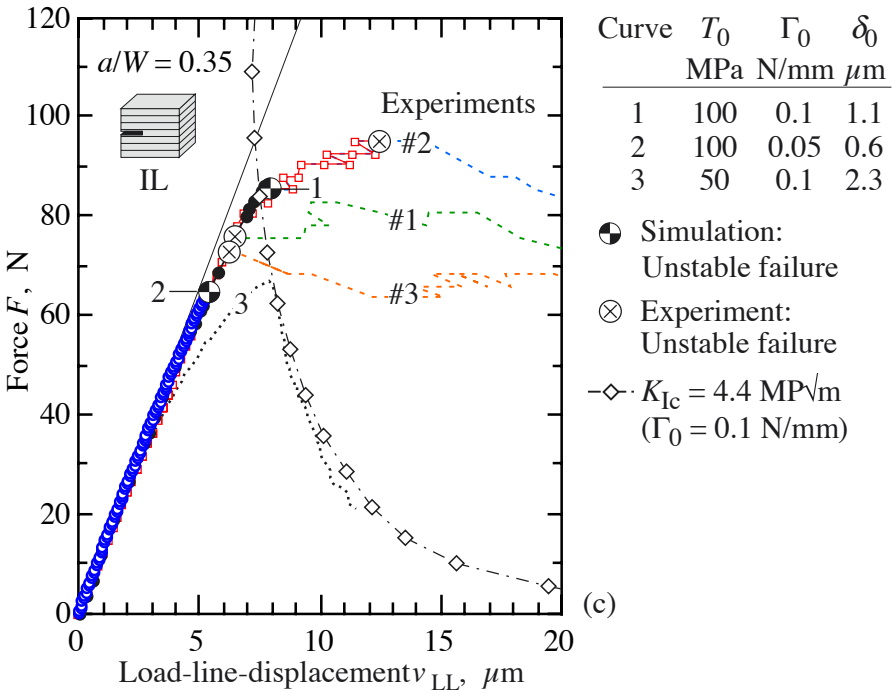
120
100
80
60
40
20
0
0
5
10
15
20
Force F, N
Load-line-displacement v_{LL}, μm
$a/W = 0.35$
IL
Experiments
#1
#2
#3
1
2
3
(c)
Curve T_0 MPa Γ_0 N/mm δ_0 μm
1 100 0.1 1.1
2 100 0.05 0.6
3 50 0.1 2.3
Simulation: Unstable failure
Experiment: Unstable failure
$K_{Ic} = 4.4$ MP$\sqrt{}$m
($\Gamma_0 = 0.1$ N/mm)

Fig. 8c

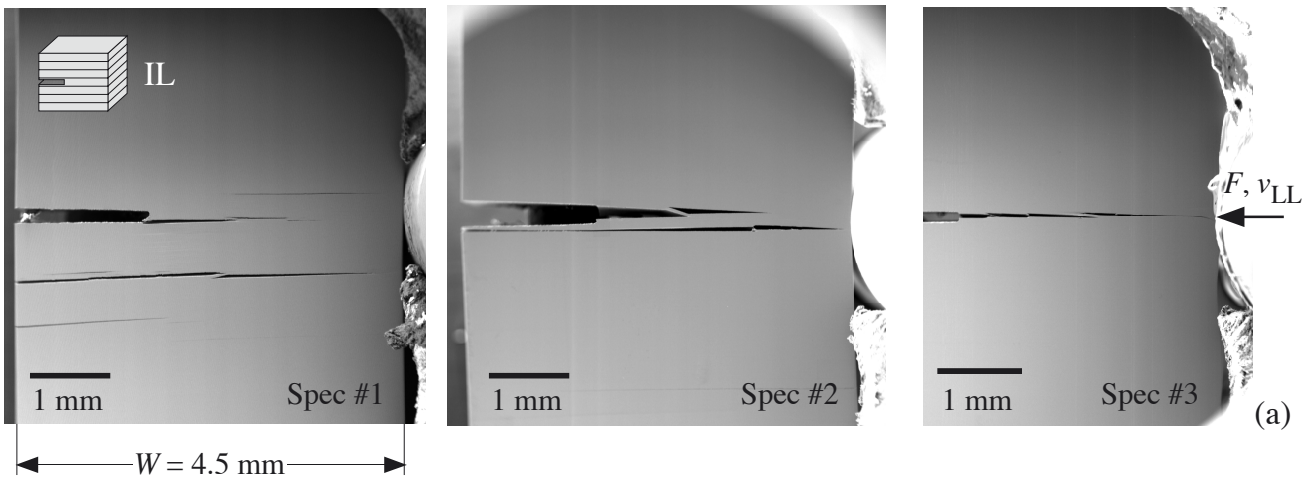
IL
1 mm
Spec #1
W = 4.5 mm
1 mm
Spec #2
F, v_LL
1 mm
Spec #3
(a)

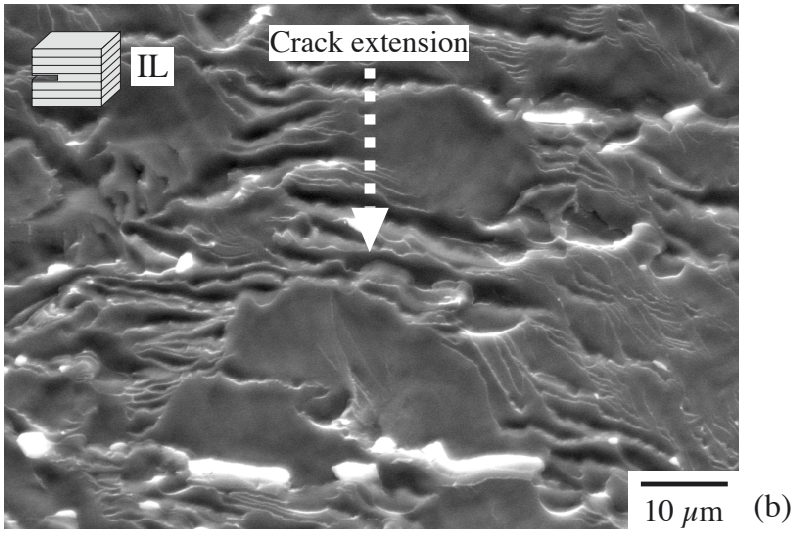
IL
Crack extension
10 μm
(b)

Fig. 9

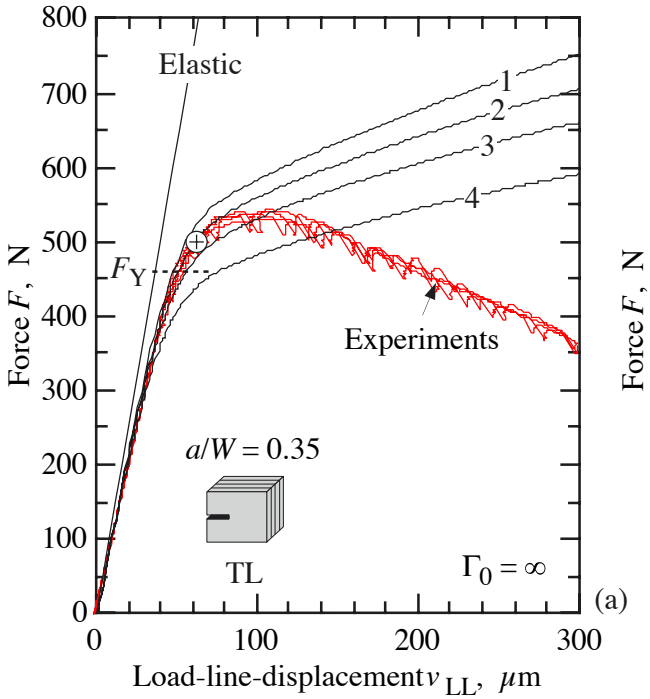

Curve	T_0 MPa	Γ_0 N/mm
1	1000	∞
2	600	∞
3	500	∞
4	400	∞

⊕ Crack initiation (exp.)

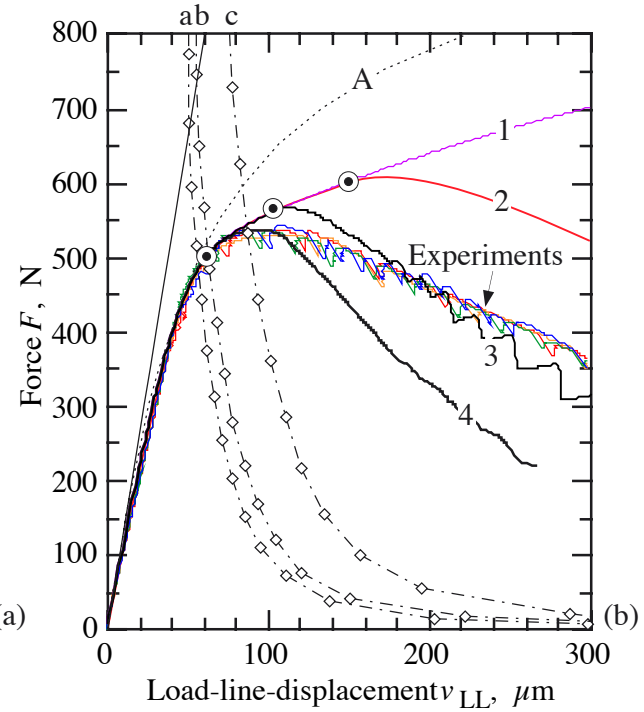

Curve	T_0 MPa	Γ_0 N/mm	δ_0 μm
1	600	∞	∞
2	600	10	19.1
3	600	6	11.4
4	600	5	9.5

⊙ Iniation followed by stable crack extension

Curve	K_{Ic} MPa$\sqrt{m}$	Γ_0 N/mm
a	31.0	5
b	33.9	6
c	43.8	10

a,b,c: Limit curves for elastic condition with K_{Ic} = constant

A: a_{eff} with $r_p = \frac{1}{2\pi}\left[\frac{K(a_0)}{\sigma_Y}\right]^2$

Fig. 10

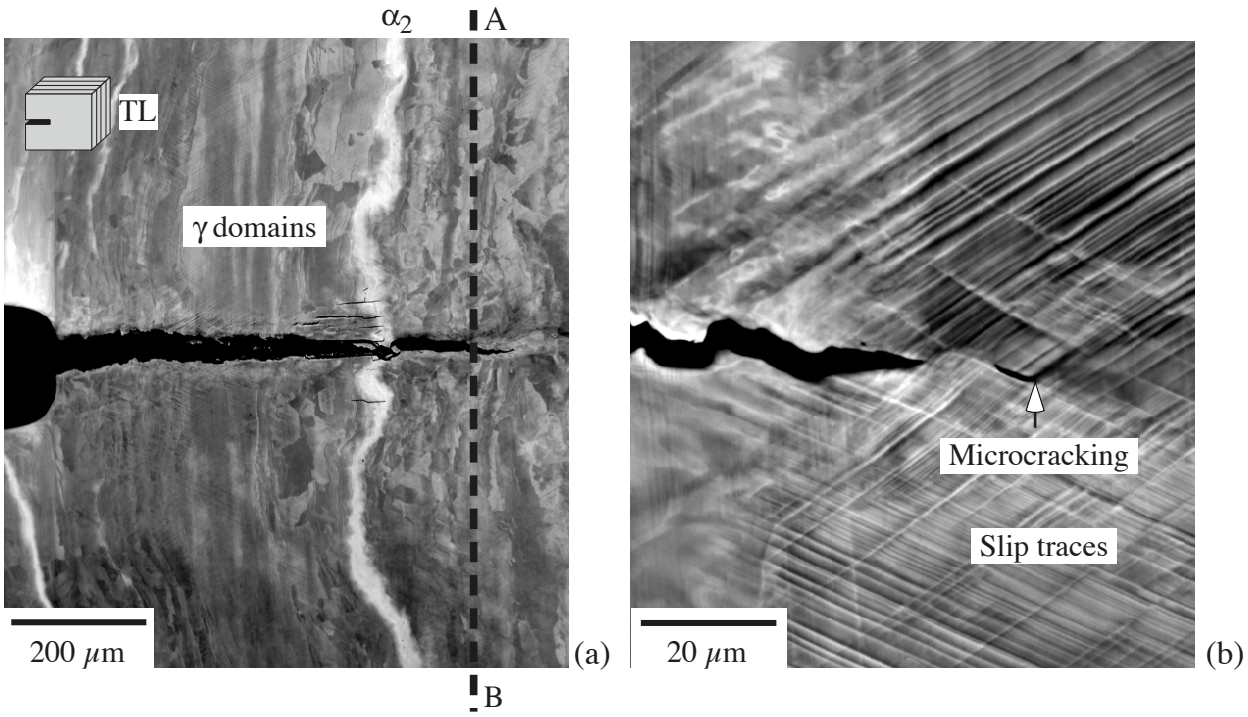

Fig. 11

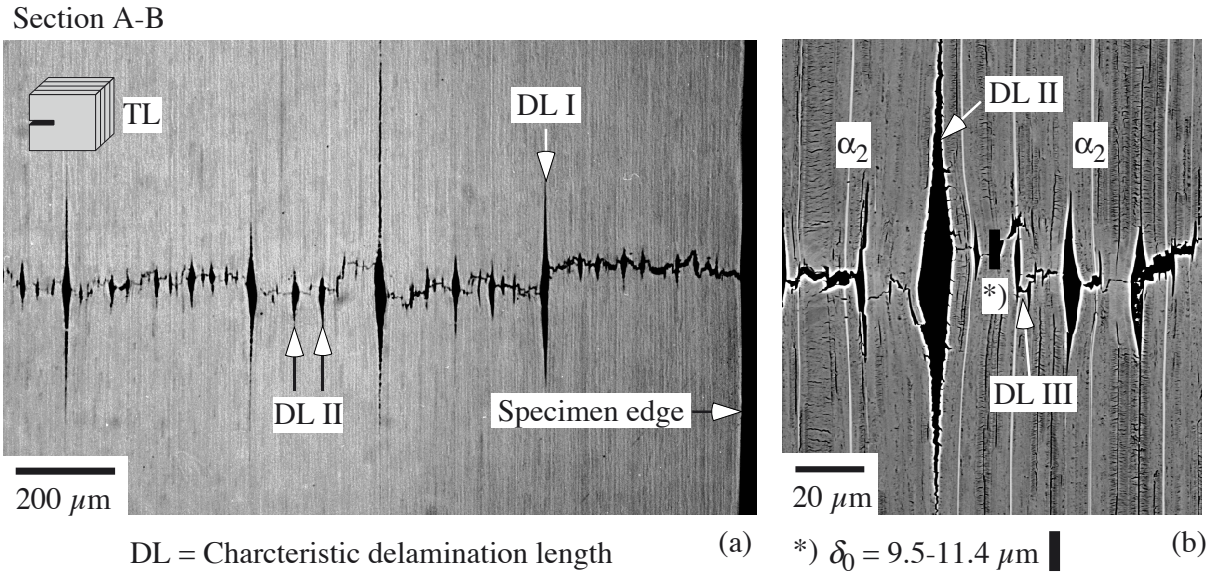

DL = Charcteristic delamination length (a)

*) δ_0 = 9.5-11.4 μm (b)

Fig. 12

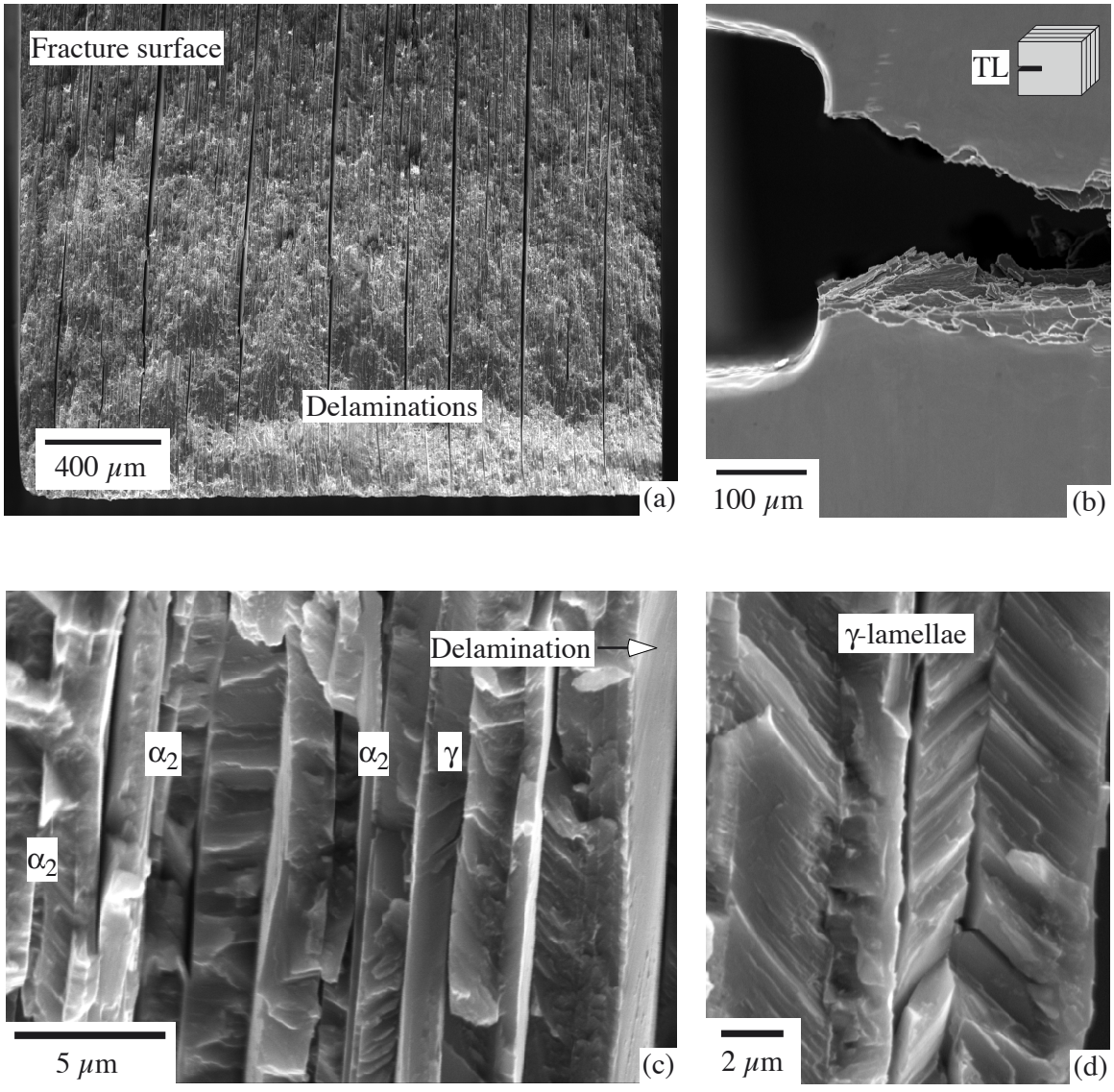
Fracture surface
Delaminations
400 μm
(a)
TL
100 μm
(b)
Delamination
α2
α2
γ
α2
5 μm
(c)
γ-lamellae
2 μm
(d)

Fig. 13

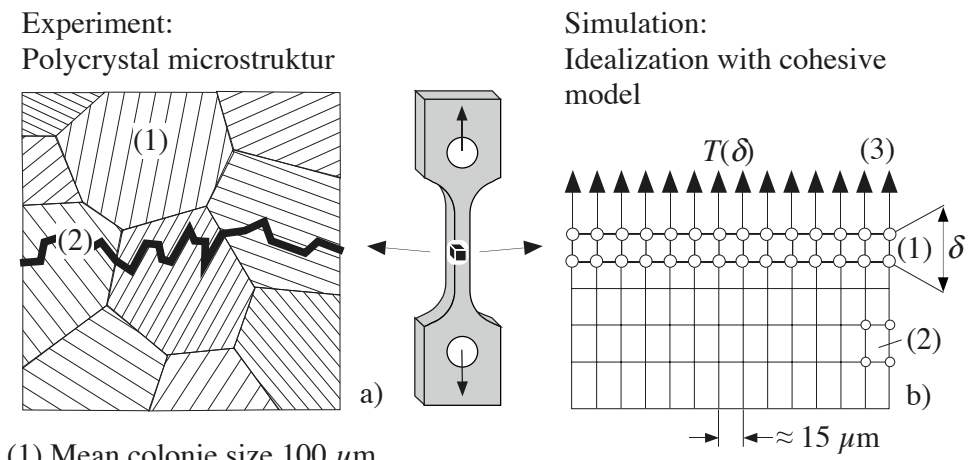

(1) Mean colonie size 100 μm
(2) Rough fracture plane

(1) Cohesive elements
(2) Solid elements, 8-noded
(3) Homogeneous parameters along cohesive interface

Fig. 14

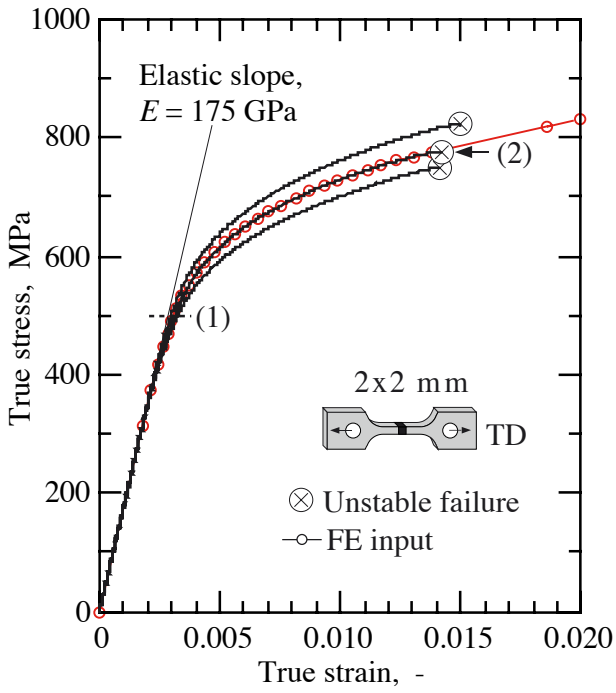

(1) Yield strength, σ_Y = 500 MPa
(2) Mean failure strength, T_0 = 780 MPa

Fig. 15

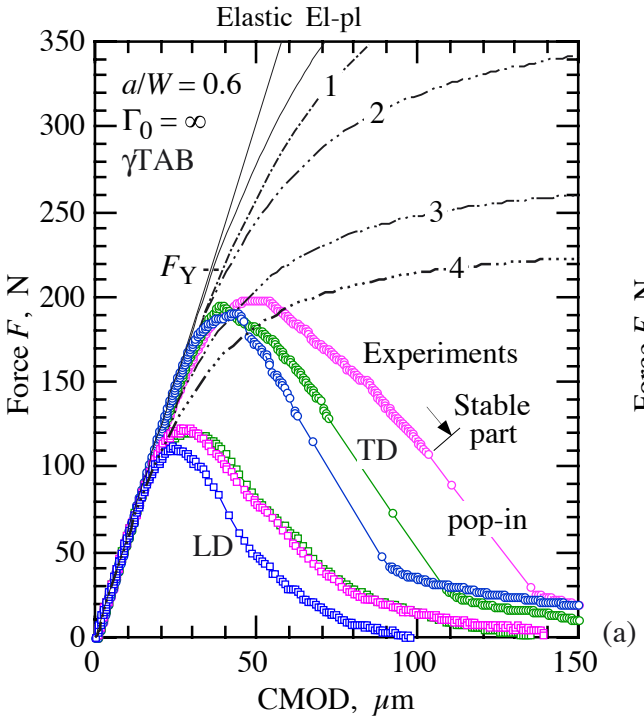

Curve	T_0 MPa	Γ_0 N/mm
1	780	∞
2	500	∞
3	400	∞
4	300	∞

Plane stress: F_Y = 217 N

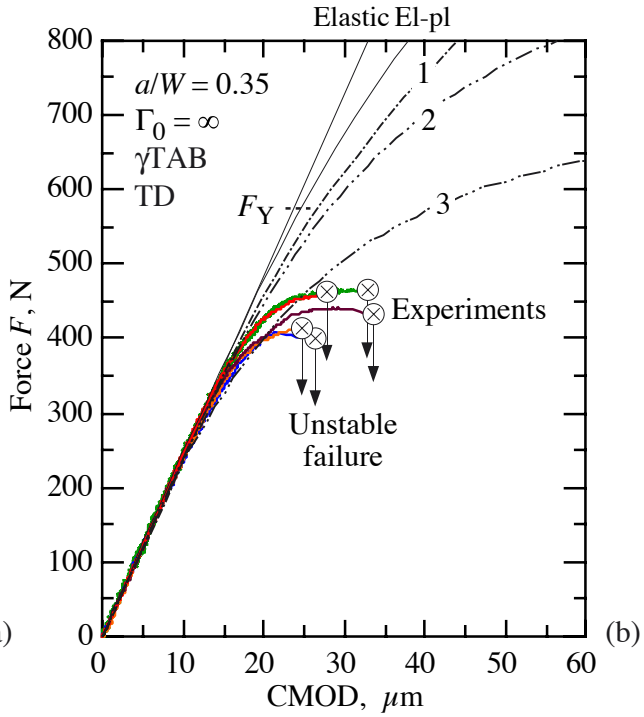

Curve	T_0 MPa	Γ_0 N/mm
1	780	∞
2	500	∞
3	400	∞

Plane stress: F_Y = 573 N

Fig. 16

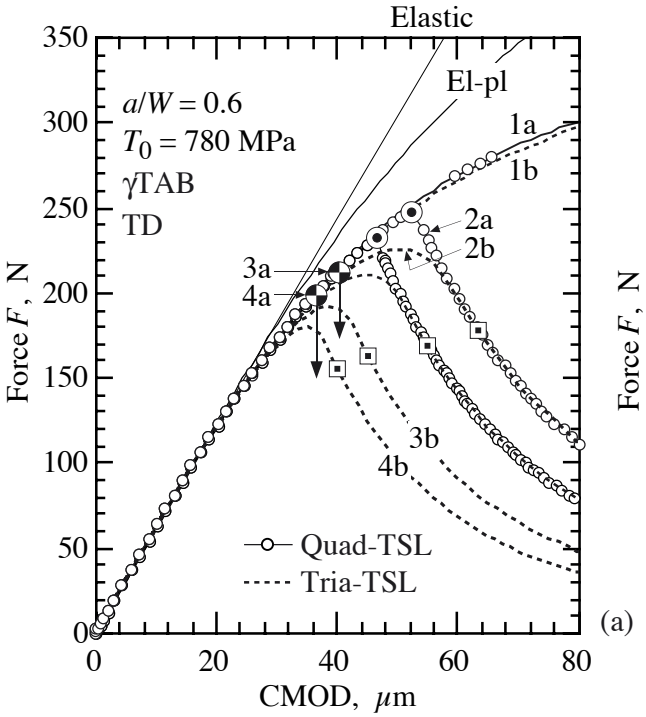

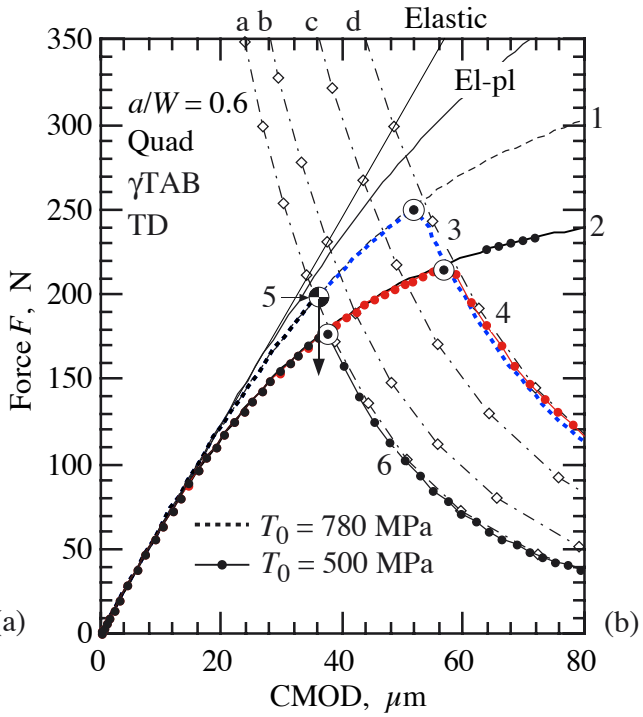

Curve	Γ_0 N/mm	TSL	Behaviour
1a	∞	Quad	Stable
2a	5.0	Quad	Stable
3a	3.0	Quad	Unstable ◓
4a	2.5	Quad	Unstable ◓
1b	∞	Tria	Stable
2b	5.0	Tria	Stable
3b	3.0	Tria	Stable
4b	2.5	Tria	Stable

◓ Unstable failure for Quad-TSL
(for T_0 = 780 MPa: $\Gamma_0 \leq$ 3 N/mm)

Curve	T_0 MPa	Γ_0 N/mm	Behaviour
1	780	∞	Stable
2	500	∞	Stable
3	780	5	Stable
4	500	5	Stable
5	780	2.5	Unstable ◓
6	500	2.5	Stable

Curve	K_{Ic} MP√m	Γ_0 N/mm
a	21.9	2.5
b	24.1	3.0
c	27.7	4.0
d	31.0	5.0

⊙ Iniation point for Quad-TSL,
followed by stable crack extension

⊡ Iniation point for Tria-TSL,
followed by stable crack extension

Fig. 17

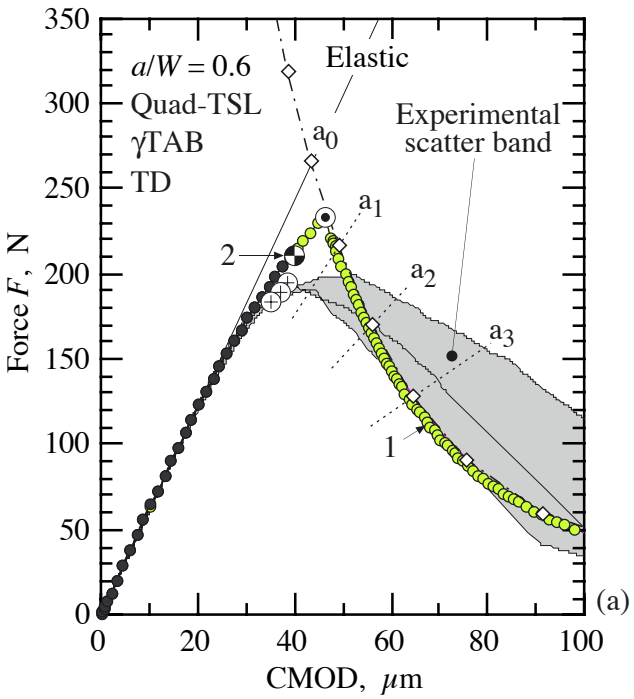

Curve	T_0 MPa	Γ_0 N/mm	δ_0 μm	TSL	Behaviour
1	780	4	5.9	Quad	Stable
2	780	3	4.4	Quad	Unstable

- Unstable failure, simulation
- Initiation, simulation
- Initiation, experiment

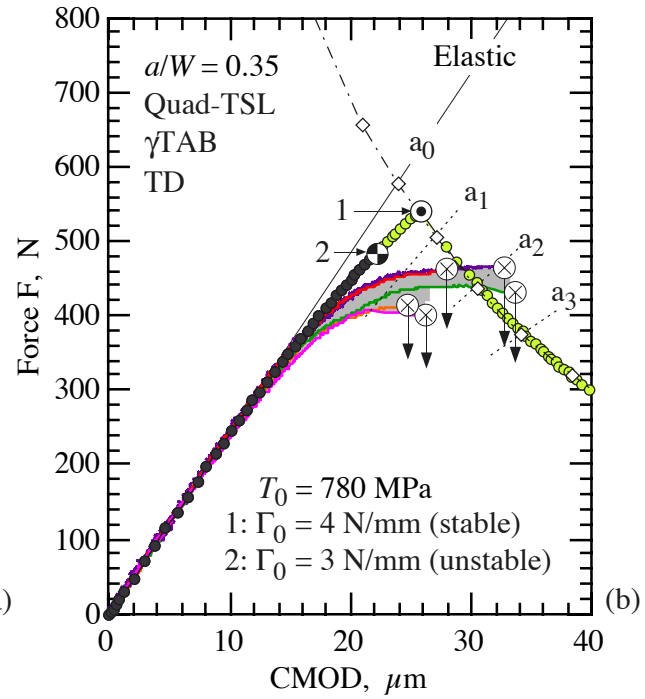

- K_{Ic} = 27.7 MP√m (Γ_0 = 4 N/mm)
- Experiments with unstable failure

Curve	Δa μm
a_0	0
a_1	225
a_2	450
a_3	675

Fig. 18

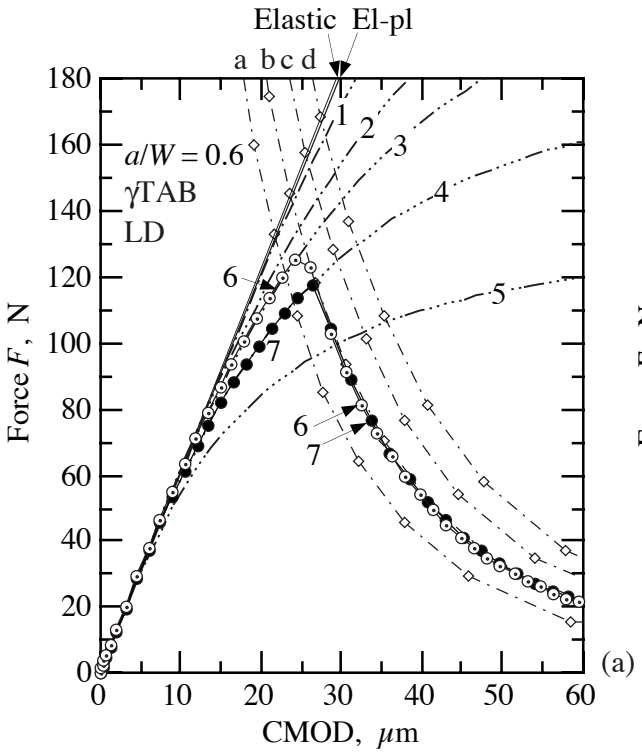

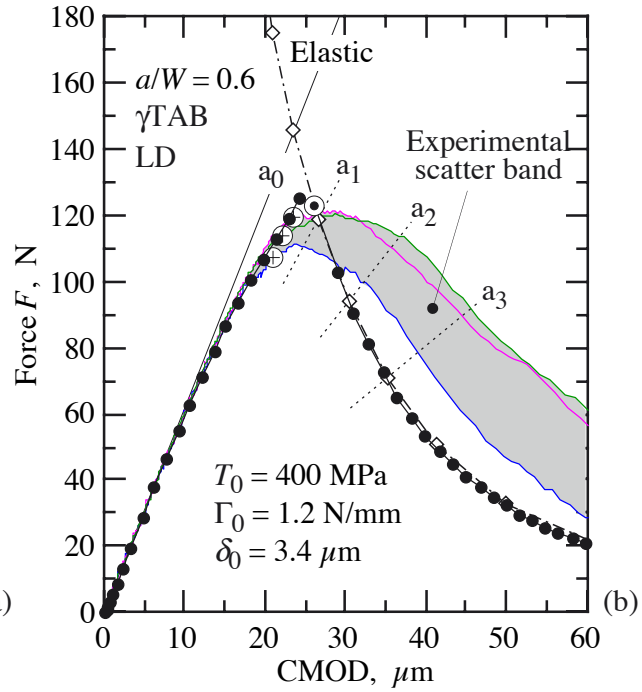

Curve	T_0 MPa	Γ_0 N/mm
1	780	∞
2	500	∞
3	400	∞
4	300	∞
5	200	∞
6	400	1.2
7	300	1.2

Stable behaviour

Curve	K_{Ic} MP√m	Γ_0 N/mm
a	13.8	1.0
b	15.2	1.2
c	16.4	1.4
d	17.5	1.6

K_{Ic} = 15.2 MP√m (Γ_0 = 1.2 N/mm)

Initiation from simulation

Initiation experiment

Curve	Δa μm
a_0	0
a_1	225
a_2	450
a_3	675

Fig. 19

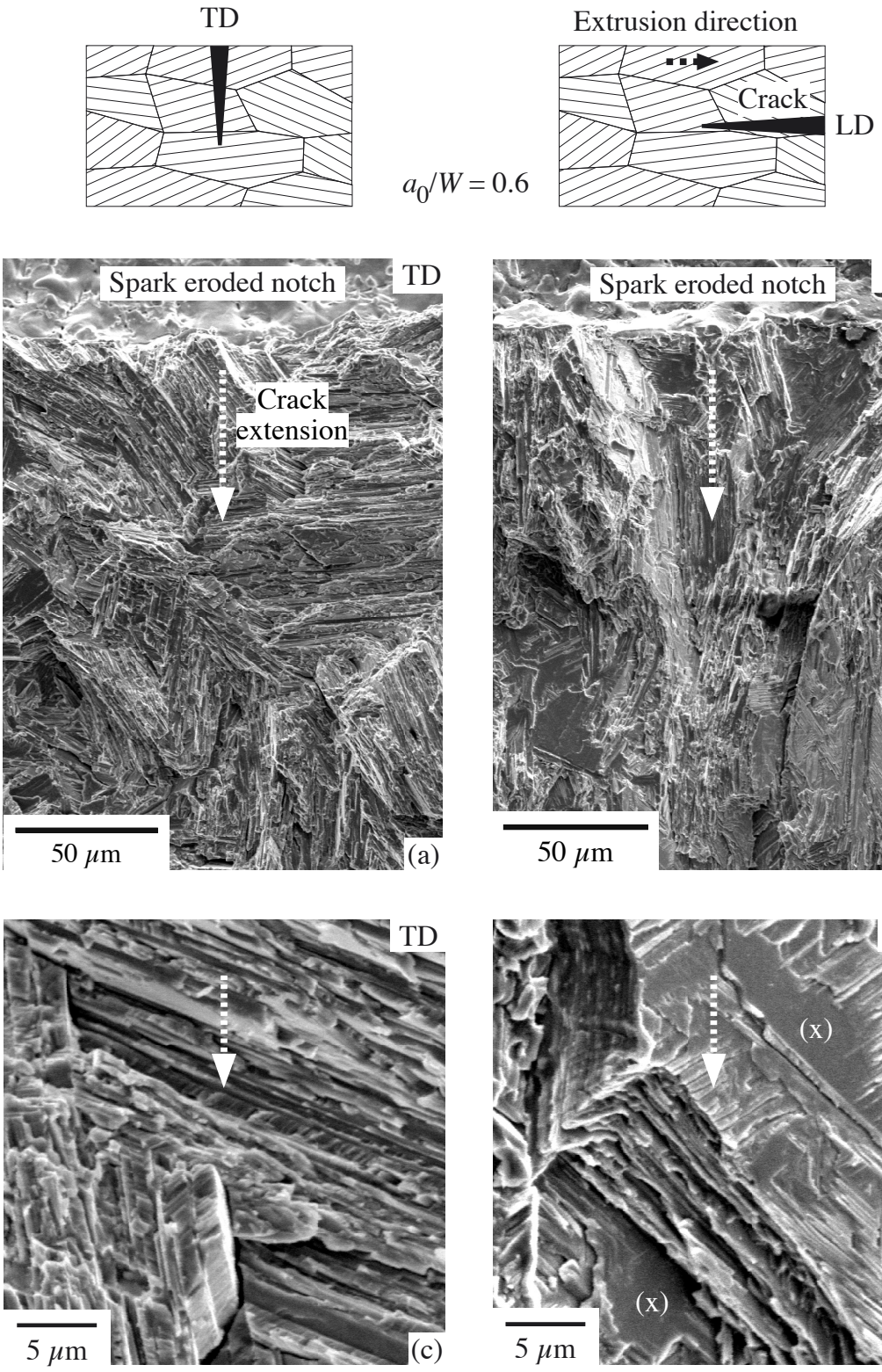
TD
Extrusion direction
Crack
LD
$a_0/W = 0.6$
Spark eroded notch
TD
Crack
extension
50 μm
(a)
Spark eroded notch
LD
50 μm
(b)
TD
5 μm
(c)
LD
(x)
(x)
5 μm
(d)

Fig. 20

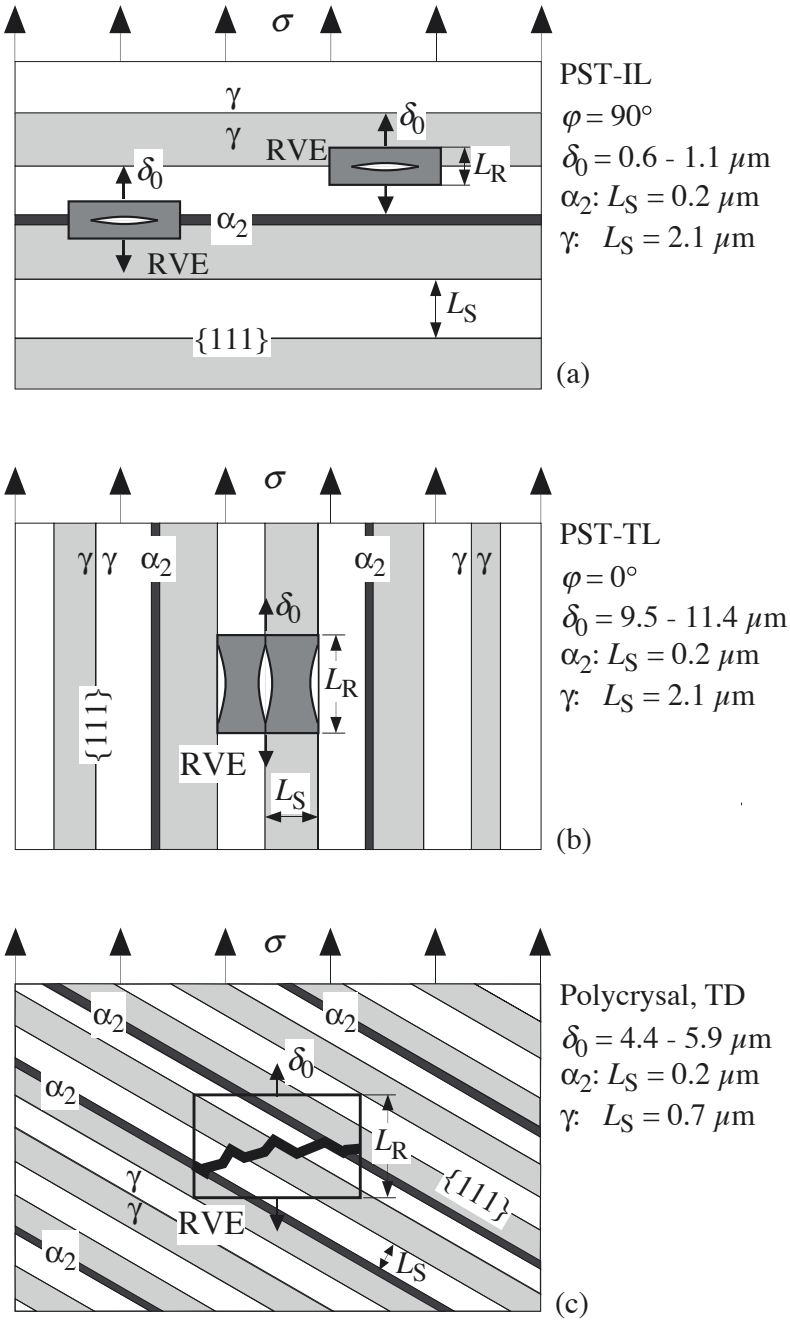
σ
γ
γ
RVE
δ0
δ0
LR
α2
RVE
LS
{111}
(a)
PST-IL
φ = 90°
δ0 = 0.6 - 1.1 μm
α2: LS = 0.2 μm
γ: LS = 2.1 μm
σ
γ γ
α2
α2
γ γ
δ0
LR
{111}
RVE
LS
(b)
PST-TL
φ = 0°
δ0 = 9.5 - 11.4 μm
α2: LS = 0.2 μm
γ: LS = 2.1 μm
σ
α2
α2
δ0
α2
LR
{111}
γ
γ
RVE
α2
LS
(c)
Polycrysal, TD
δ0 = 4.4 - 5.9 μm
α2: LS = 0.2 μm
γ: LS = 0.7 μm

Fig. 21